BASIC RESEARCH IN CRYSTALLINE AND NONCRYSTALLINE CERAMIC SYSTEMS

Department of Materials Science and Engineering
Ceramics Division
Massachusetts Institute of Technology
Cambridge, Massachusetts 02139

ANNUAL REPORT

For the Period August 1, 1979 to October 31, 1980

Prepared for:
U.S. Department of Energy
Under Contract No. DE-AC02-76ER02390

DISCLAIMER

BASIC RESEARCH IN CRYSTALLINE AND NONCRYSTALLINE CERAMIC SYSTEMS

Department of Materials Science and Engineering
Ceramics Division
Massachusetts Institute of Technology
Cambridge, Massachusetts 02139

ANNUAL REPORT

For the Period August 1, 1979 to October 31, 1980

Prepared for:

U.S. Department of Energy

Under Contract No. DE-AC02-76ER02390

DISTRIBUTION OF THIS DOCUMENT IS UNLIMITED

TABLE OF CONTENTS

Table of Contents (Continued)

INTRODUCTION

The Basic Research Programs in Ceramics sponsored by the U.S. Department of Energy supports a significant fraction of the research effort and graduate student training in ceramics at M.I.T. Various research subjects have been investigated in the past, including heat conduction, surface characteristics, diffusion in oxides, high temperature kinetic processes, microstructure development, effects of microstructure on properties, the structure and properties of noncrystalline ceramics, dissolution kinetics, materials preparation, and solid-vapor reactions. This report presents results of the current research program.

The program this year has been supervised by Professors W. D. Kingery, R. L. Coble and R. M. Cannon. The experimental work is performed largely by graduate students working toward advanced degrees, along with technicians and research staff. Supervising staff members and students are identified for each research project described in this report. All work has been planned by the Principal Investigators.

The importance of basic research programs in ceramics processing and properties is becoming widely recognized as the critical role of improved ceramic materials for energy systems is acknowledged. The needs identified in the 1977 series of workshops on DOE programs in energy-related materials research and by the ongoing efforts of the DOE Council on Materials Science are being translated into the basic and applied research necessary to fulfill the established objectives in the effort to solve the nation's energy problems. Present indications are that ceramics in numerous applications will be critical in meeting national energy requirements.

1.0 Electrical, Optical and Dielectric Properties

1.1 Ionic Conductivity and Mg Vacancy Mobility in MgO

Personnel: D. R. Sempolinski and W. D. Kingery

Most conduction phenomena in MgO have been examined using temperature, oxygen pressure and aliovalent solute content as independent variables. To separate the ionic and electronic conductivities, both the DC conductivity and the ionic transference number (the fraction of current carried by the ionic species) were measured over the same temperature and oxygen pressure ranges. To evaluate aliovalent solute effects, the samples used in this study were doped so that a single element controlled the defect structure; i.e., the concentration of one impurity element was increased to a level which overwhelmed the background impurity effects. By this approach a correspondence was established between the dominant solute and observed changes in either the ionic or electronic conductivity. The experimental apparatus is shown in Figure 1.1.1.

MgO is found to be a mixed conductor with ionic and electronic conductivities of the same order of magnitude. Data from several diffusion and photo-Hall effect studies indicate that for MgO the electronic species are on the order of 10^7 times more mobile than the ionic species. The only way, therefore, that an ionic species can have a conductivity comparable to that of the electronic species is if its concentration is roughly 10^7 times greater. That is, under all conditions the concentrations of electronic defects are negligible as compared to the concentrations of ionic defects.

For MgO, the controlling charge balance equation which fixes the ionic defect structure appears to be

$$2[V''_{Mg}] = [I^{\bullet}_{Mg}] + [Fe^{\bullet}_{Mg}] \quad ,$$

where $[V''_{Mg}]$ is the concentration of magnesium ion vacancies, $[I^{\bullet}_{Mg}]$ is the concentration of the fixed-valence solutes such as Al and Sc, and $[Fe^{\bullet}_{Mg}]$ is the concentration of Fe^{+3}. This relationship conforms to site-balance requirements

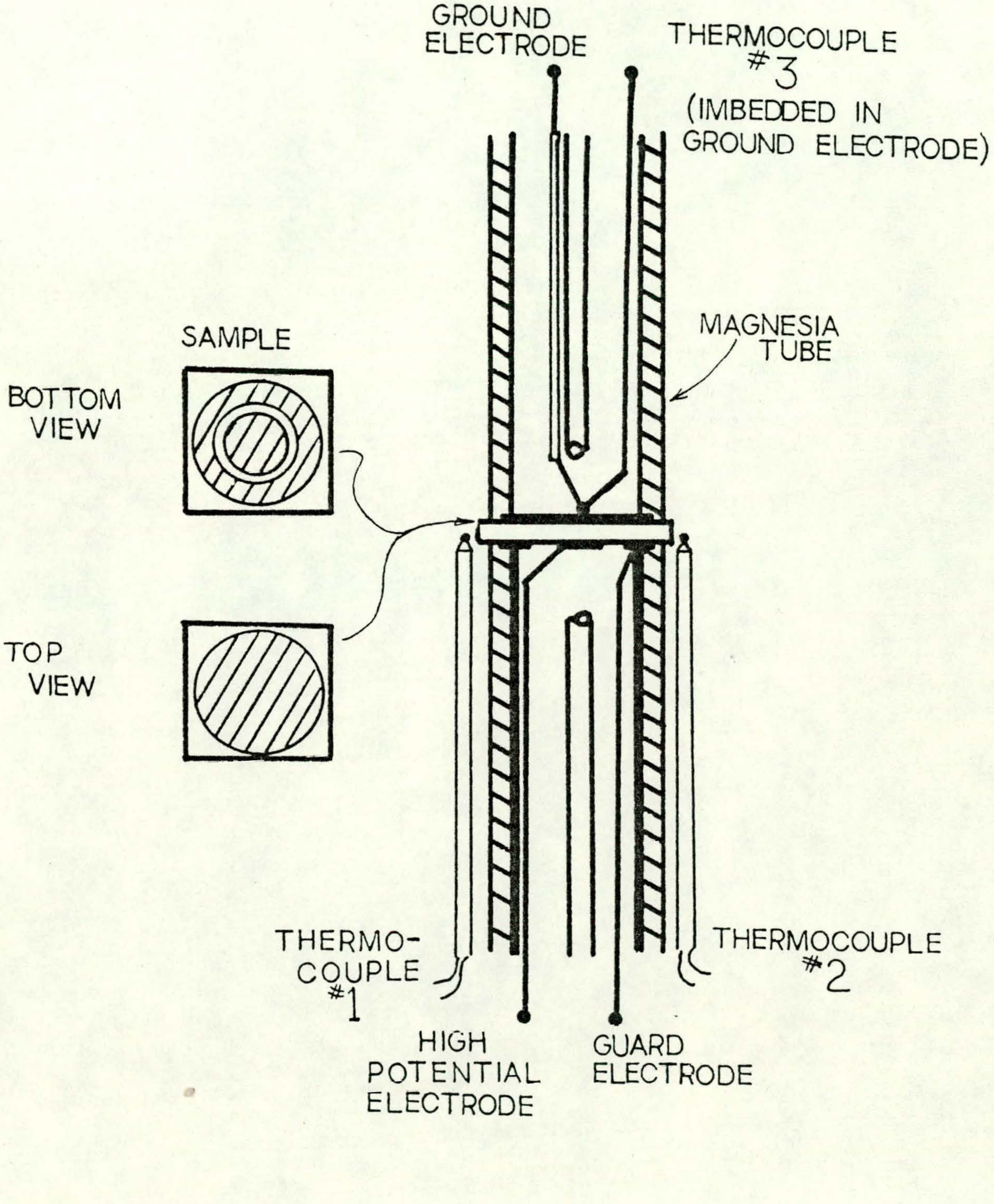

Figure 1.1.1 Experimental apparatus - sample holder and elctrode configuration.

and the high energies required for interstitial ion formation. V''_{Mg} is the charge compensating species formed when a trivalent solute is introduced into the MgO lattice. At the temperatures and dopant concentrations used in this study, association effects between aliovalent solute ions and vacant sites can be neglected. (This is not true for the Sc-doped sample at lower temperatures, as will be described below.) The assumption that V''_{Mg} is the ionic charge carrier is confirmed by our findings that the ionic conductivity is directly proportional to the trivalent solute content and that the activation energy for ionic conductivity is independent of the specific trivalent dopant.

Since the concentration of V''_{Mg} is known from the doped level, its mobility can be calculated from the ionic conductivity data using the general relation

$$\sigma = (Ze)n\mu$$

where n is the carrier concentration, Ze is its charge and μ is its mobility. The results of such a calculation using the data of the OR, Al-400 and Sc-1500 samples are shown in Figure 1.1.2. The equal values found for carrier mobility in samples ranging from 65 to 1500 ppm solute is an added confirmation of our theory.

A least-square fit analysis of the data shows that the temperature dependence of the ionic mobility can be expressed as

$$\mu_{V''_{Mg}} = 2 \exp\left(-\frac{2.13\ \text{eV}}{kT}\right) = \frac{8800}{T} \exp\left(-\frac{2.27\ \text{eV}}{kT}\right) .$$

From this result, the diffusion coefficient of the magnesium vacancy was obtained,

$$D_{V''_{Mg}} = (0.38 \pm 0.15) \exp\left[-\frac{2.27 \pm 0.2\ \text{eV}}{kT}\right]$$

using the Nernst-Einstein equation.

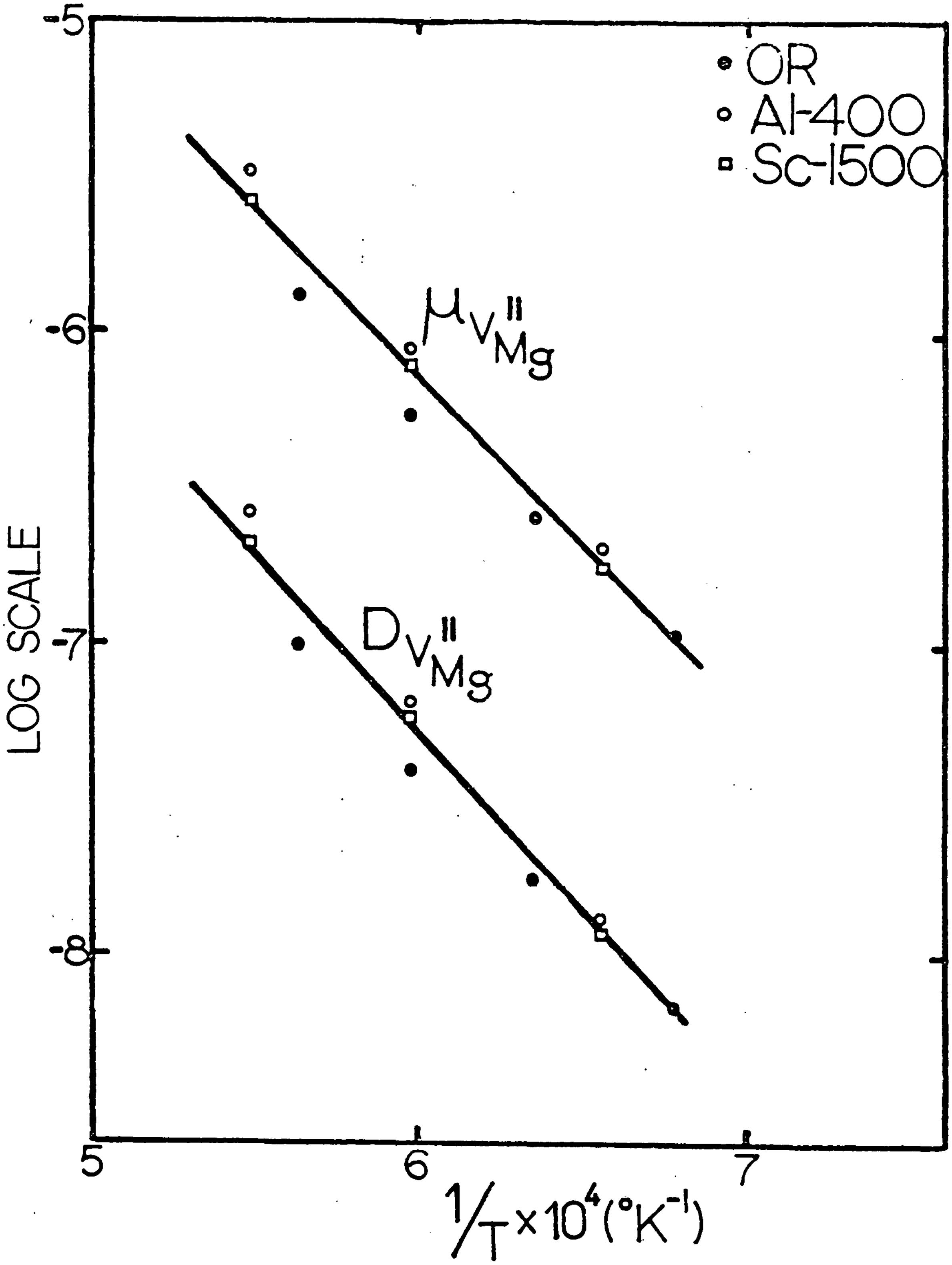

Figure 1.1.2 Mobility and diffusion coefficient of V''_{Mg} as a function of temperature.

The entropy of motion, ΔS_M, can be estimated from the pre-exponential term, D_o, using the relation

$$D_o = \gamma \lambda^2 \nu \exp\left(\frac{\Delta S_M}{k}\right),$$

where γ is a geometric factor of order unity, λ is the jump distance, and ν is the atomic viabrational frequency. Since for MgO λ is approximately 2×10^{-8} cm and ν is 1.3×10^{13}/sec, it follows that

$$\frac{\Delta S_M}{k} = 4.3 \ .$$

The diffusion coefficient of the magnesium ion, D_{Mg}, can also be calculated from the expression for $D_{V''_{Mg}}$ by using the equation

$$D_{Mg} = [V''_{Mg}]D_{V''_{Mg}} = [\frac{I_{TOTAL}}{2}]D_{V''_{Mg}} \ .$$

D_{Mg} values determined in this manner are the solid lines displayed in Figure 1.1.3. They agree well with the measured D_{Mg} values (the data points in Figure 1.1.3) in magnitude and, in fact, suggest that the scatter observed in the measured diffusion data is the result of differences in the impurity concentrations of the samples used in those studies. Chemical analysis showed that the diffusion samples measured contained only several hundred ppm of aliovalent impurities. We infer that impurities were picked up during the experiment from the tracers used or from the furnace atmosphere.

The activation energies determined from the high-temperature magnesium ion diffusion data are consistent with the 2.27 eV value observed in this study. We do not believe that experimentally difficult diffusion measurements with so many possible sources of contamination in a contaminant-sensitive material should be over-interpreted.

1.2 Electronic Conductivity in Single Crystalline MgO

Personnel: D. R. Sempolinski, W. D. Kingery and H. L. Tuller

Our previous report determined that the magnesium vacancy is the

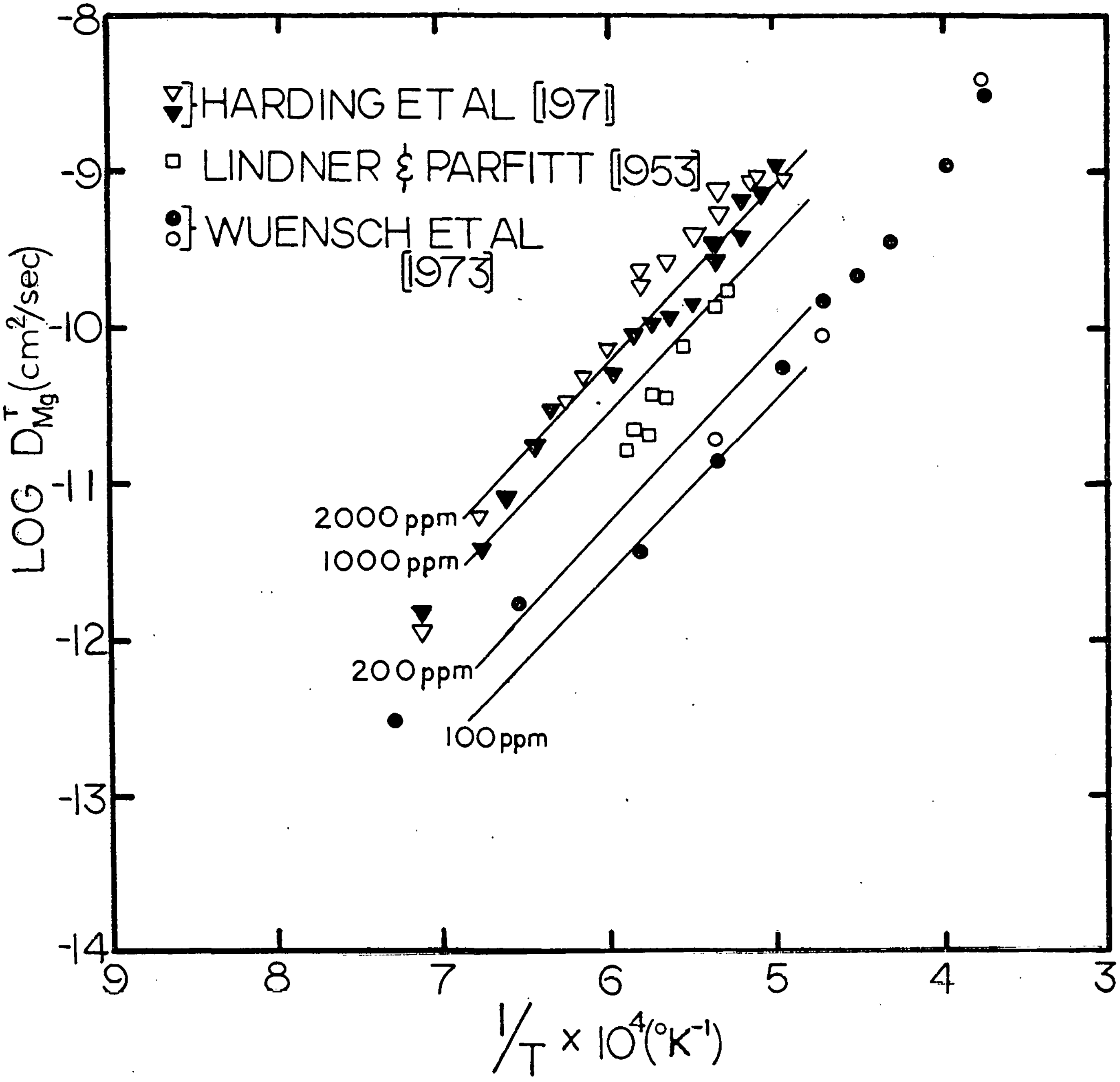

Figure 1.1.3 Comparison of measured D_{Mg} values (data points) to those calculated from $D_{V''_{Mg}}$ expression (solid lines).

predominant ionic charge carrier and that the defect structure is governed by the charge balance condition

$$2[V''_{Mg}] = [I^{\bullet}_{Mg}] + [Fe^{\bullet}_{Mg}] \quad ,$$

where $[V''_{Mg}]$, $[Fe^{\bullet}_{Mg}]$ and $[I^{\bullet}_{Mg}]$ are the magnesium vacancy, trivalent iron and fixed trivalent solute (e.g., Al or Sc) concentrations, respectively. Since electrons and holes are about 10^7 times more mobile than ionic defects, the observation of a mixed conduction process implies that the concentrations of electronic defects must be negligible in comparison to those of ionic species. That is, the electronic conductivity in MgO provides a direct way of studying defects which do not control the defect structure.

The DC conductivity and ionic transference numbers were measured over a temperature range of 1200-1600°C and an oxygen pressure range of 10^{-1} - 10^{-13} MPa for all samples. The electronic conductivity, σ_{elec}, was determined from these data using the equation

$$\sigma_{elec} = \sigma_o(1 - t_i) \quad ,$$

where σ_o is the total conductivity and t_i is the ionic transference number. For each composition the electronic conductivity shows a minimum as a function of oxygen pressure centered at approximately 10^{-5} to 10^{-8} MPa, which suggests the occurrence of a p to n-type transition. The slopes of the log σ_{elec} versus P_{O_2} curves range from +1/5.6 to +1/4 at high oxygen pressure and from -1/5 to -1/4 at low oxygen pressures. The temperature dependence of electronic conduction is also similar for all compositions. At high oxygen pressures, where holes are the predominant electronic carrier, the activation energy is 300±15 kJ/mol, while at low oxygen pressures, where electrons are the majority electronic species, its value is 365±15 kJ/mol. This suggests that the same conduction processes occur in all samples.

The mass balance equations shown in Table 1.2.1 are derived from expressions for equilibration with the atmosphere, valence change of iron, electron hole generation, the mass balance equation for iron and the mass

Table 1.2.1 Listing of defect reactions and mass balance conditions.

Reaction		Mass Action Relation
Atmospheric equilibration	$\frac{1}{2}O_2 \rightarrow V_{Mg}'' + O_O + 2h^{\bullet}$	$k_{ox} = \frac{[V_{Mg}''] \, p^2}{P_{O_2}^{1/2}}$
Electron-hole generation	$\text{null} \rightarrow e' + h^{\bullet}$	$k_e = pn$
Valence changes of iron	$Fe_{Mg}^{x} \rightarrow Fe_{Mg}^{\bullet} + e'$	$k_{Fe} = \frac{[Fe_{Mg}^{\bullet}] \, n}{[Fe_{Mg}^{x}]}$
Mass balance equation for iron	$Fe_{TOTAL} = [Fe_{Mg}^{x}] + [Fe_{Mg}^{\bullet}]$	
Mass balance equation of fixed trivalent impurities	$I_{TOTAL} = [I_{Mg}^{\bullet}]$	

Note: Kroger-Vink notation used.

$Fe_{TOTAL} \equiv$ total iron concentration

$I_{TOTAL} \equiv$ total fixed trivalent solute concentration.

$p \equiv$ hole concentration.

$n \equiv$ electron concentration

Sempolinski, Kingery and Tuller
Table 1.2.1

balance equation for all fixed valence trivalent impurities. From these relations,

$$(Fe_{TOTAL} \frac{k_{Fe}}{k_e})\ p^3 + (I_{TOTAL})\ p^2 = 2k_{ox}\ P_{O_2}{}^{1/2} .$$

This relation indicates that the hole concentration should vary as $P_{O_2}{}^{1/6}$ if at low oxygen pressure the $Fe^{\bullet}_{Mg}$ concentration (accounted for by the first term on the left side of the equation) is still larger than that of the fixed trivalent solutes, and as $P_{O_2}{}^{1/4}$ if it is smaller. Ionic conductivity data for the Fe-320 sample indicate that the intermediate case ($I_{TOTAL} \simeq [Fe^{\bullet}_{Mg}]$) exists in the low oxygen pressure regime. This suggests that the hole concentration should vary roughly with a $P_{O_2}{}^{1/5}$ dependence and the electron concentration with a $P_{O_2}{}^{-1/5}$ dependence.

If holes are the predominant electronic species at high oxygen pressures and electrons at low oxygen pressures, the above analysis indicates that the electronic conductivity should vary at high oxygen pressures with a $P_{O_2}{}^{1/4}$ dependence for all the samples and at low oxygen pressures with a $P_{O_2}{}^{-1/4}$ dependence for the OR, Al-400 and Sc-1500 samples and a $P_{O_2}{}^{-1/5}$ dependence for the Fe-320 sample. This behavior is in good accord with our observed results.

The significance of the charge balance condition can be further appreciated by considering its consequences from the viewpoint of the energy band structure. Figure 1.2.1 gives a schematic representation of the band gap in MgO. The width of the band gap is based on the results of optical studies, which indicate that it is within the range 710 to 760 kJ/mol (7.4 to 7.9 eV/electron). The energy level of V''_{Mg} was determined using available optical data and that of Fe^{x}_{Mg} is based on data which suggest that the iron level is approximately in the middle of the band gap. The position of the I^{x}_{Mg} center is in accord with a coulombic attraction calculation, which gives an ionized energy of roughly 50 to 100 kJ/mol (0.5 to 1.0 eV/electron).

I^{x}_{Mg} and Fe^{x}_{Mg} are un-ionized donor states and V''_{Mg} and V'_{Mg} are acceptor levels. (Labeling of the energy levels follows the convention that the symbol of a given level indicates the state of the defect if that level is occupied.)

Sempolinski, Kingery and Tuller
Figure 1.2.1

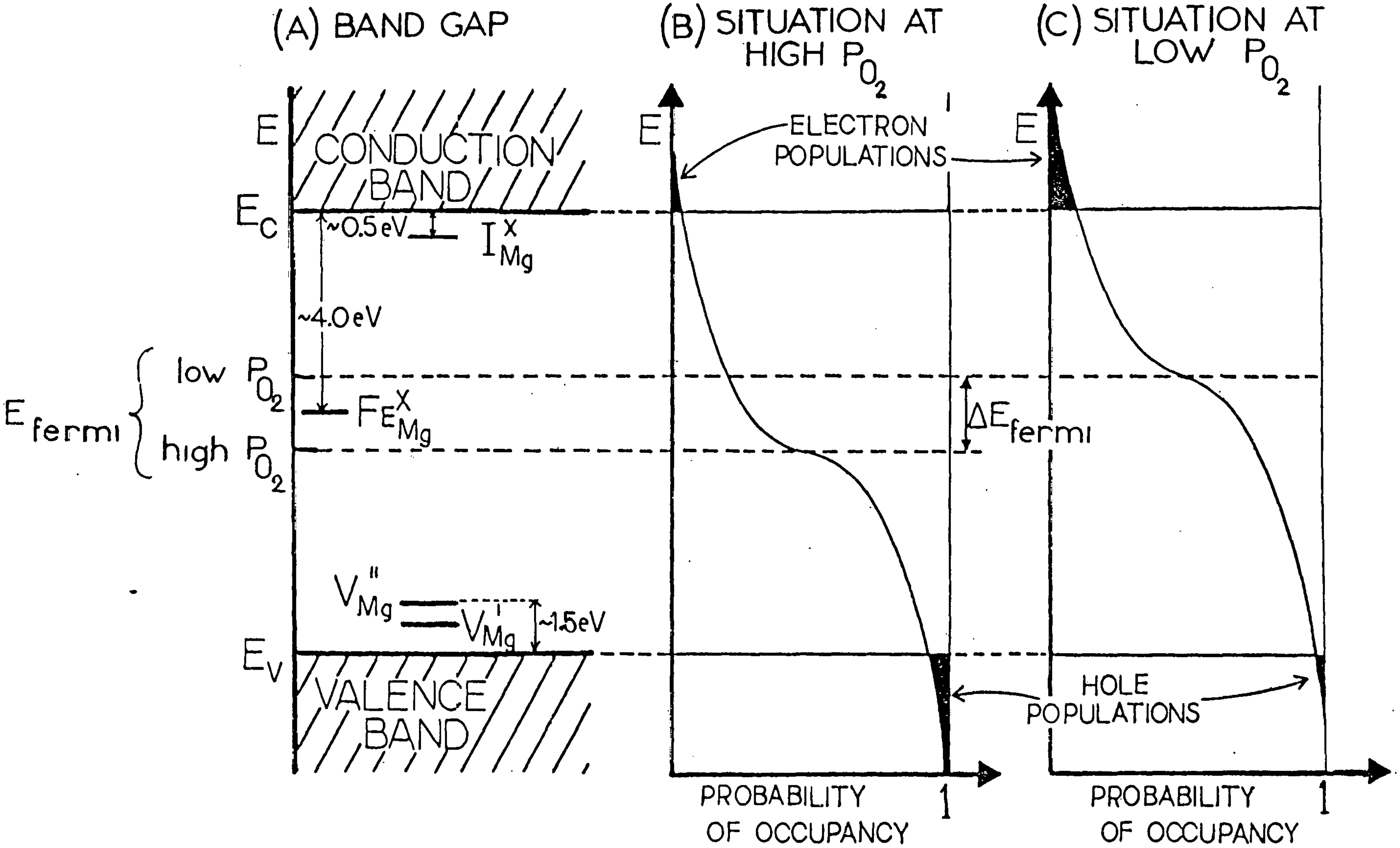

Figure 1.2.1 (a) Schematic diagram of thermal band gap for MgO; (b and c) shift in fermi level and elctron distribution as function of P_{O_2}.

Since the energies of the donor states are greater than those of the acceptor states, compensation occurs. The overall energy of the system is lowered by having the electrons shift from the donor to the acceptor levels. Moreover, since the charge balance condition requires that the number of the donor and acceptor states is equal, compensation is complete. That is, magnesium vacancies and solute ions cancel out each other's effects as donor and acceptor species.

This compensation phenomenon explains several of the observed features of the electronic conductivity process. Since compensation is complete, the fermi level is not pinned to any specific solute level but rather remains very near its intrinsic position. It is for this reason that the activation energies of the electronic conductivity do not vary greatly with the specific solute. In addition, since the energy of the V''_{Mg} acceptor is less than that of the lowest energy donor state, it, and not the singly ionized V'_{Mg}, is the stable state of the magnesium vacancy.

The oxidation process is but a small perturbation from the completely compensated state since the concentrations of electronic species are so much smaller than those of ionic defects. Since the holes are a minority species, oxidation leads to orders of magnitude changes in their concentration and in the electronic conductivity while having virtually no effect on the charge balance condition and ionic conductivity.

For the Fe-320 sample, the introduction of holes results in a shifting of the fermi level towards the valence band. Since the Fe^x_{Mg}/Fe_{TOTAL} ratio is a measure of the probability that the Fe^x_{Mg} is occupied, its change as a function of oxygen pressure can be used to calculate the shift in the fermi level. It follows from Fermi-Dirac statistics that the change in the fermi level with oxygen pressure is

$$\Delta E_{fermi} = kT \ \ell n \left\{ \frac{\dfrac{Fe_{TOTAL}}{[Fe^x_{Mg}]_{P_{O_2}'}} - 1}{\dfrac{Fe_{TOTAL}}{[Fe^x_{Mg}]_{P_{O_2}''}} - 1} \right\} .$$

The Fe^{x}_{Mg}/Fe_{TOTAL} ratio is known from the ionic conductivity data. At 1400°C, it varies roughly from 0.14 in pure oxygen to 0.75 at 10^{-7} MPa of O_2. These numbers reveal that the fermi level passes through the Fe^{x}_{Mg} state at some point during the oxidation process and show that the shift in the fermi level is roughly 6.4×10^{-20} J (0.4 eV). Although this is only a small change, it does indicate that the concentrations of the holes and electrons are increased and diminished respectively by roughly a factor of 20 over the stated oxygen pressure range. For MgO, such shifts in concentrations of the electronic species, when weighted by the difference in the mobilities, are enough to make an n to p transition possible.

The described defect structure provides a good qualitative picture of the conduction processes in MgO and has been used for a more detailed analysis of the conductivity data. The results of two different calculations are: first, an examination of the temperature dependence of the electronic conductivity minima from which values for the thermal band gap and mobilities of the electronic species are obtained; second, a derivation of specific expressions for the defect reaction constants using parameters determined in the first calculation.

From the temperature dependence of the minimum in electronic conductivity, a value of 650 kJ/mol (6.8±0.5 eV/electron) is derived for the thermal band gap. Electron and hole mobilities of about 24 and 7 $cm^2/V\cdot sec$, respectively, at 1673°K are derived. Estimates of about 600 and 200 $cm^2/V\cdot sec$ for room temperature electron and hole mobility are higher than previous estimates, suggesting that additional scattering modes are predominant at lower temperatures.

Equilibrium constants for defect reactions involving oxidation have been derived. Calculated hole concentrations at 1673°K decrease from $9\times10^{12}/cm^2$ in pure oxygen to 5×10^{10} at $P_{O_2} = 10^{-10}$ MPa. Calculated electron concentrations increase from $2\times10^{9}/cm^2$ in pure oxygen to $3.4\times10^{11}/cm^2$ at $P_{O_2} = 10^{-10}$ MPa. Calculated changes of electronic conductivity from the quantitative model are in good accord with experimental data for each of the compositions studied.

1.3 Modification of the Permittivity of MgO by Aliovalent Solutes and Dislocations

Personnel: J. M. Driear and W. D. Kingery

The complex permittivity has been measured from 100 Hz to 100 kHz between room temperature and 850° in a sample holder, specially designed for use over this temperature and frequency range. Each isothermal permittivity response curve has been modeled as the sum of a background conductivity, a major relaxation of the Cole-Cole type, and two minor peaks of the Debye type flanking the major peak at higher and lower frequencies. Samples doped with chromium and iron were measured, as well as undoped samples, some of which were deformed.

Measuring the complex permittivity as a function of applied frequency and temperature allows the bulk conductivity as well as the A.C. relaxations to be studied. By analyzing the changes in the relaxation frequency and dispersion of the loss peak, the energies of formation and motion of the defect responsible for the peak may be simultaneously obtained. Because some concentration data is available from the dispersion, kinetics may be studied. Analysis of the conductivity term yields an energy which may be correlated with the results of D.C. conductivity and diffusion work.

There are, however, problems associated with such measurements since the dispersion depends on the product of the size of the relaxing defect and its concentration. Hence, small concentration of large defects may be detected and only with difficulty identified. The two factors may be separated only by using ancillary information such as the energy of ordering of a cluster.

The conclusions reached are:

(1) Three broad regions of behavior were identified in MgO. Below 600°C, a region of limited mobility exists in which defect structures can not transform into their equilibrium form. Samples quenched into this region retain most of their high temperature defect structure. Above 600°C and below 1200°C, sufficient mobility exists for short-range equilibration, and clusters of defects or precipitation of solutes may occur in times of several hours. Above 1200°C, simple defect associates predominate.

(2) Samples had anomalously high permittivity after electrode application which annealed out completely at about 600°C and did not reappear. The loss increased as the kinetic energy of the impinging platinum atoms increased, leading us to conclude that the anomaly is caused by near-surface damage. Sputtered platinum electrodes were shown to be blocking for all experimental conditions in this work.

(3) The measured complex permittivity consisted of a background conductivity and a broad relaxation. The broad relaxation was modeled as the sum of a major relaxation of the Cole-Cole form flanked at lower and higher frequencies by two relaxations of the Debye form. Attempts were made to model the background conductivity as space charge build-up at the electrodes or as an inhomogeneous planar layer. Since neither was successful, a simple frequency-independent bulk conductivity was used.

(4) The background conductivity was analyzed in terms of the contributions from three species. Magnesium vacancies appear to dominate the defect structure under low-iron or reducing conditions. Conduction has an experimental activation enthalpy of 2.7 eV. Under high-iron and oxidizing conditions, the dominant defect is ferric iron, and iron defect conduction probably occurs through iron-vacancy dimer interchanges. The measured enthalpy of motion was 2.1±0.1 eV. At low temperatures or under low iron-vacancy dimer concentrations, a third species is observed which has an energy of motion of 1.1 to 1.2 eV. This was identified as the same defect that was responsible for the major Cole-Cole peak.

(5) Under oxidizing conditions, the major Cole-Cole peak has an enthalpy of motion of 1.15±0.05 eV and a formation energy of 0.1±0.05 eV. The active defect for this relaxation was tentatively identified as tetrahedrally-coordinated Mg ions in a spinel precipitate or cluster, which are not permanently associated with a vacancy. Using the decrease in the energy of motion when a sample doped with 2850 ppm of iron (4N2300) was reduced, the concentration of this defect at 780°C was determined to be 315 ppm, and the jump size was calculated at 0.40 MgO lattice spacings - quite close to the 0.42a expected for octahedral to tetrahedral jumps.

(6) Interpretation of the Debye relaxation proved to be quite difficult. Both the complexity of the defect response and the large amount of experimental

noise in the data made positive identification of the defect responsible for the relaxation impossible. A pair of octahedrally coordinated vacancies surrounding a tetrahedrally coordinated solute ion was hypothesized by analogy to work done in wustite. Assuming that each complex makes it impossible for another complex to occupy adjacent sites, the low temperature, high frequency Debye relaxation was tentatively identified as interchanges between equivalent tetrahedral sites; the high temperature, low frequency relaxation was identified with octahedral-tetrahedral interchanges.

(7) Deformation modified the dielectric properties of the crystal in a manner akin to decreasing the concentration of aliovalent solutes. A comparison of the effect of deformation to the effects of iron or chromium solutes suggested that dislocations decrease the number of available tetrahedrally-coordinated sites in the crystal.

1.4 Galvanic Cell Measurements with Stabilized Zirconia and Platinum Probes

Personnel: N. J. Dudney and R. L. Coble

For metal oxides which are electronic or mixed conductors, typical techniques for measuring the transference numbers at high temperatures are often inadequate. Many techniques are only useful in setting limits for these parameters, because the effects are too small for accurate measurements. Others are plagued with experimental difficulties, such as the necessity for hermetic seals, or uncertainties in the sample composition and possible interference from unwanted polarizations and transport paths.

For example, a classic Faraday experiment, where mass transport is measured when a current is passed through the sample, becomes very difficult when oxygen is the element that must be monitored. Blocking electrode measurements also present serious problems. Measurements with a thick metal electrode to block the ionic component of the conductivity are inaccurate when the ionic transference number is small. Alternatively, the use of an electrolyte to block the electronic transport can give an accurate measurement of a small ionic transference number, but requires the use of ionic probes which may be awkward. In both blocking electrode techniques, interaction of the cell components with the gas phase may short circuit the blocking effect and must be prevented. For an oxide, this interaction with the surrounding atmosphere is difficult to avoid while maintaining control of the sample composition by control of the gas phase composition.

Another technique which is frequently used to measure the ionic transference number for oxides is a galvanic cell measurement. This involves establishing a gradient in the chemical potential of oxygen across the sample and measuring the open circuit voltage with metal probes. This works very well for measurements of an ionic conductor; however, when the sample is an electronic or mixed conductor, the open circuit potential may be too small for a reliable measurement and surface polarization problems are more likely to affect the measurements.

Weppner and Huggins described a variation of the galvanic cell technique which uses ionic conductors as probes rather than the conventional metal probes. Wagner used this technique for measurements of Ag_2S, but the method has never been applied to the high temperature measurements of oxides. When ionic conducting probes are used in combination with metal probes, there are several important advantages; the cell potentials can be accurately measured for both ionic and electronic conductors, there is an internal check for surface polarization problems, and the cell is relatively easy to construct and operate.

The derivation of the potential measured by ionic probes in a galvanic cell is analogous to that for metal probes. The theoretical results show that the polarity is opposite to that measured by metallic probes, because they sense the chemical potential of electrons rather than oxygen.

The galvanic cell technique has been tested by measuring the ionic and electronic transference numbers of metal oxides at high temperatures. The cell uses stabilized zirconia probes in addition to the conventional metal probes. With both types of probes, measurements of the transference numbers for electronic, ionic or mixed conductors are possible and surface polarization effects are readily detected. Measurements of yttria doped ceria and urania have demonstrated the advantages of the technique over the available methods. The signs of the voltages measured with the respective probes are opposite to one another, in accordance with the theory. Also, both materials show evidence that the leakage currents are partially controlled by surface reactions in some of the ranges of P_{O_2}, particularly when the difference in P_{O_2} across the cell is large. This is manifested by respective transference numbers that give sums smaller than unity.

1.5 Electrical and Optical Properties of Ceramics

Personnel: R. French and R. L. Coble

Many problems in transport and conductivity of Al_2O_3 can be solved by a detailed understanding of its electronic structure. Through the use of High Temperature Vacuum Ultraviolet (VUV) Spectroscopy coupled with Solid State Bank Theory and Molecular Orbital theory one can determine the temperature dependence of the band gap, the electronic carrier concentration, and the defect states introduced by impurities, vacancies and interstitials. The previous effort in this area was hindered by a poor signal to noise ratio along with contamination problems. A systematic investigation has been undertaken in collaboration with Hans Jenssen of the Crystal Physics Group here at M.I.T. to deal with these problems. The aim is to develop a spectrophotometer capable of operation up to 1500°C in the wavelength range of 900 to 2000 Å (14 to 6 eV) in both reflection (near normal incidence) and transmission modes. Work at wavelengths longer than 2000 Å can be done on the high temperature Cary 14 spectrometer.

The present work has concentrated on the vacuum system and heating method, the optical layout and detector are also being redesigned. The Hydrogen discharge lamp must be operated in the windowless mode because the lowest window cutoff is 1050 Å. This means there will be a substantial hydrogen leak into the system necessitating differential pumpint of the lamp. To operate in the VUV one must have a clean vacuum of 5×10^{-5} torr. To this end the vacuum system has been overhauled, cleaned and foreline traps and an improved liquid nitrogen trap have been installed. The pumping configuration has been changed so that the monochromator is directly pumped. If this is not sufficient, a turbomolecular pump with alumina absorption pumps will be considered as a solution to the oil problem.

The heating of the sample is to be done with a 75 to 100 watt CO_2 gas laser. This method has been used with great success by Tom Yager in his EPR spectroscopy work. There are many advantages; the optical distances in both transmission and reflection can be kept small so more light is collected, while power dissipation and black body radiation is minimized. Also, A CO_2 laser eliminates the need for a furnace in the vacuum system, thereby avoiding two major contamination problems; outgassing of the furnace and vapor deposition of volatile impurities from the furnace onto the sample. Preliminary tests on 1 cm^2 sapphires have been conducted, while more extensive tests of sample mounts are planned. Heat flow calculations have been done to determine the power needed.

The signal to noise ratio is being increased by many means. The monochromatic light is to be chopped at 400 hz and will be discriminated from the background by lock-in techniques. An Osmium coated mirror will be used in the system so as to have converging optics, therefore, the detector can be placed near the focal point, allowing collection of the maximum amount of VUV without much black body radiation. The use of a phosphor and light pipe is being reconsidered at this point. It has the advantage of simplicity, but, in this application, the conversion of VUV to blue and then detection of blue light means one is actually detecting in a spectral range where the black body radiation in orders of magnitude more intense. If, instead, one uses a windowless electron multiplier or channeltron with an appropriate photocathode (e.g. CsI), the signal to noise ratio is much greater. A problem is that the quantum efficiency of these detectors is low.

Various optical layouts are being considered. One involves tilting the mirror and moving the detector through 180° to get incident versus transmitted or reflected light. It is not known at present if it is feasible to move the detector, but matched detectors are unavailable. Another method would use a reference sapphire or mirror. This would be very sensitive to temperature shifts in the spectra.

2.0 Kinetic Studies

2.1 Defect Equilibria of OH^--related Defects in MgO

Personnel: K. W. Cheng and W. D. Kingery

The study of OH^--related defects in MgO was found to be important in understanding the nature of irradiation damage in MgO. Henderson and Sibley (B. Henderson and W. A. Sibley, J Chem. Phys. 55, 1276 [1971]) studied the isochronal annealing characteristic of OH^--related defects in MgO by IR spectroscopy. They started with a slow cooled sample and annealed the sample at subsequently higher temperatures. They found that the absorption peak heights changed with annealing temperature: the 3296 cm^{-1} peak increased and the 3700 cm^{-1} peak decreased. The 3296 cm^{-1} band in MgO has been assigned to the $V_{OH}-$ center (or V''_{Mg}-$OH^{\bullet}_{o}$), and the 3700 cm^{-1} has been assigned to brucite precipitates (or $Mg(OH)_2$). Henderson and Sibley interpreted this as the result of the solution of brucite in MgO creating $V_{OH}-$ defects. There are reasons to believe their conjecture. If a brucite crystal is put into a MgO matrix, they form a coherent interface along the basal plane of the brucite hydroxyl ions. The solution of brucite to form MgO takes place along a coherent interface in which the (110) planes in brucite become the (111) planes in MgO. That is, the dissolved hydroxyl layers become the (111) planes of MgO with the oxygen ions substituted by OH^- ions. The vacant layer of octahedral sites of brucite becomes a layer of vacant magnesium sites in MgO, charge compensating the hydroxyl ions. The result is that the MgO lattice was doped with OH-V-OH complexes or $OH^{\bullet}_{o}$-V''_{Mg}-$OH^{\bullet}_{o}$). This neutral complex will further dissociate into the singly associated defect $V_{OH}-$ and an isolated OH^-. At higher temperatures, one would anticipate seeing the further dissociation of the singly associated $V_{OH}-$ to an isolated OH^- and a cation vacancy. These reactions can be written as:

$$Mg(OH)_2 \text{ ppt} \longrightarrow \text{OH-V-OH}$$

$$\text{OH-V-OH} \longrightarrow V_{OH}- + OH^{\bullet}_{o}$$

$$V_{OH}- \longrightarrow V''_{Mg} + OH^{\bullet}_{o} \; .$$

Henderson and Sibley's interpretation of their annealing results are in qualitative agreement with the above crystal chemistry analysis. Henderson and Sibley isochronally annealed the crystal for 10 minutes. It is not certain whether the system had equilibrated in the short 10 minute anneal. We repeated Henderson and Sibley's experiment by performing isochronal anneals of 1 hr and 24 hrs on two sets of crystals, which had been slow cooled from 1000°C. The results of the isochronal anneals are similar to those of Henderson and Sibley.

When brucite dissolves in MgO forming OH-V-OH, the equilibrium can be expressed as:

$$K_1 = [\mathrm{OH\text{-}V\text{-}OH}] \quad .$$

The absorption peak of OH-V-OH in IR is not known; therefore, we cannot measure [OH-V-OH] directly. Since one mole of brucite dissolved gives one mole of OH-V-OH, the change in brucite concentration can be used to measure the amount of change in [OH-V-OH]. A plot of the ln $\{[\text{brucite}]_{\text{max}} - [\text{brucite}]_T\}$ vs. 1/T should give us a straight line with slope of $-\Delta H_{\text{solution}}/k$ (See Fig. 2.1.1).

For the dissociation of OH-V-OH into V_{OH}^- and OH, the equilibrium can be expressed as

$$K_2 = \frac{[V_{OH}^-][\mathrm{OH}]}{[\mathrm{OH\text{-}V\text{-}OH}]} \quad .$$

Here, we cannot measure [OH] and [OH-V-OH] directly, because their absorption peaks are unknown. Since one mole of OH-V-OH dissociates into one mole of V_{OH}^- and one mole of OH, we can use the change in $[V_{OH}^-]$ to measure the amount of change of [OH-V-OH] and [OH]. The equilibrium K_2 can thus be expressed as

$$K_2 = \frac{[V_{OH}^-]^2}{[V_{OH}^-]_{\text{max}} - [V_{OH}^-]_T} \quad .$$

A plot of ln K_2 v. 1/T should give a straight line with slope of $-(\Delta H_{\text{solution}} + \Delta H_{\text{dissociation}})/k$ (See Fig. 2.1.2).

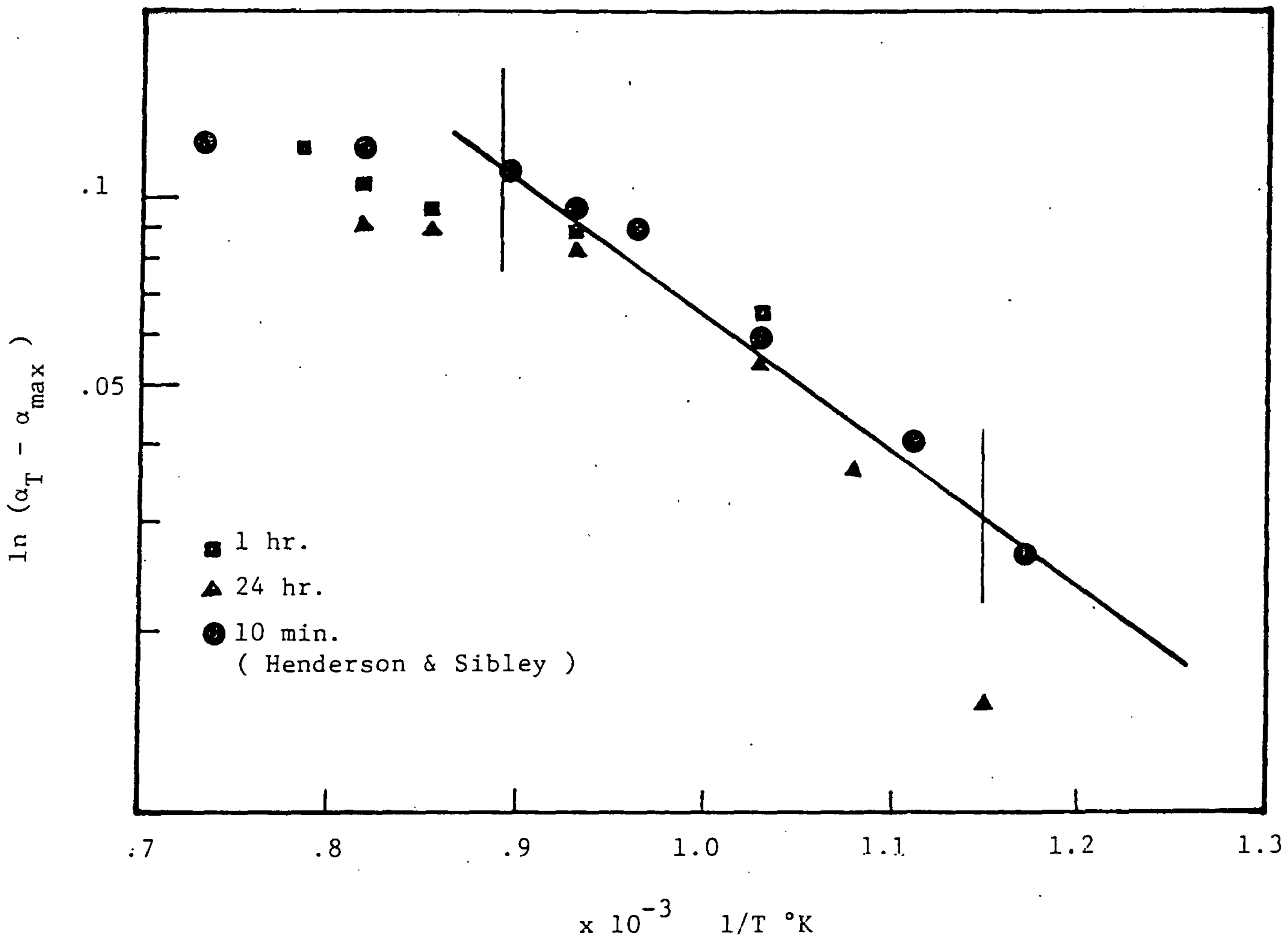
.1
.05
ln (α_T - α_{max})
■ 1 hr.
▲ 24 hr.
● 10 min.
(Henderson & Sibley)
.7
.8
.9
1.0
1.1
1.2
1.3
x 10^{-3} 1/T °K

Figure 2.1.1

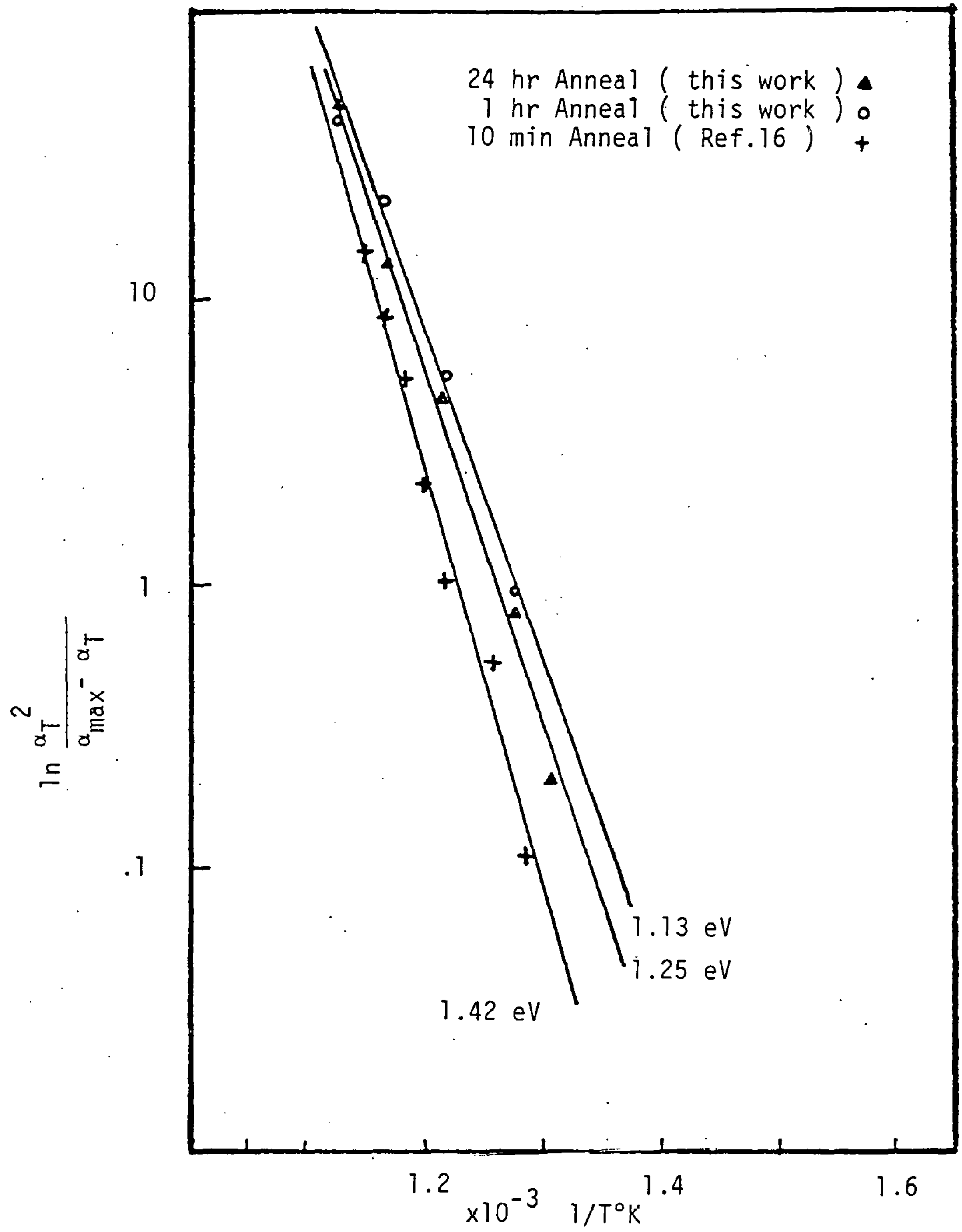

Figure 5.20 Plot of the $\alpha_{3296\ \mathrm{cm}^{-1}}$ by Equation 5.57

Figure 2.1.2

As shown in these two figures, the data between 600 to 850°C fitted a straight line fairly well. From this, a heat of solution of brucite in MgO of 0.45 eV is obtained. The dissociation energy of OH-V-OH is found to be 0.85 eV. This dissociation energy can be estimated by Coulombic calculation assuming the $OH_o^{\bullet}$ and V_{Mg}'' to be point charges. The calculated value by this simple Coulombic attraction is ∿ 1.05 eV and is in fair agreement with the experimental value.

We have attempted to continue this heat and quench isochronal study to temperatures above 1100°C, so that we could study the $V_{OH}-$ dissociation reaction. However, we found this to be a nonquenchable reaction. Also, OH diffuses out of the crystal at these temperatures. In short, the results of the isochronal annealing study are consistant with the defect reactions described in the above.

2.2 Redox Kinetics of Fe Ions in Simple Crystalline MgO

Personnel: K. W. Cheng and W. D. Kingery

The oxidation of Fe ions in MgO has been a topic of study for a number of years, and it is generally agreed in the literature that oxidatidation can be described by the reaction

$$\tfrac{1}{2}O_2 + 2Fe_{Mg}^{x} \longrightarrow 2Fe_{Mg}^{\bullet} + V_{Mg}'' + O_o \quad .$$

Previous workers have suggested that the kinetics of this oxidation reaction may be influenced by:

(1) the presence of dislocations,

(2) the association of cation vacancies and Fe^{3+} ions, and

(3) the presence of OH^- ions.

The objective of our study is to find out the rate controlling species in the redox reaction of Fe ions in single crystalline MgO with different iron contents and dislocation densities.

The effective diffusivity of hydroxyl ions in MgO was also measured. It was obtained from the rate of loss of the hydroxyl ions as a function of time and temperature.

For the iron redox kinetcs study two kinds of crystals were used: The Norton crystals (containing ∿110 ppm Fe) and the Fe-3250 crystals (containing ∿3250 ppm Fe). The concentration of ferric ions was monitored either by the 4.3 eV absorption band of the Fe^{3+} ion in UV or by the isolated Fe^{3+} line with EPR spectroscopy.

The redox kinetics were also studied on deformed undoped Norton crystals. The Norton crystals were deformed by two methods. One was hot-forged in a hot press. A total of 37% deformation was obtained by this technique. The other was deformed by 3-point bending. A total of ∿6% deformation was obtained by this technique.

The oxidation kinetics of the Norton crystals, deformed Norton crystals, and the Fe-3250 crystals were found to obey bulk diffusion laws. The oxidation rates were found to be identical to the reduction rates in the range of oxygen partial pressures chosen. The rate of loss of the hydroxyl ions was found to be identical to the oxidation rate of the Fe ions in undoped Norton crystals. These results are summarized in Figure 2.2.1 and below:

<u>Fe-3250 crystals</u>

Dislocation density, $N_d = 5\times10^5/cm^2$
Subgrain size = 0.24 mm
$\tilde{D} = 5.2 \exp(-2.52\ eV/kt)\ cm^2/sec$

<u>Norton crystals</u>

a) 3-point bent sample
   $N_d = 8\times10^5 cm^2/sec$ in the undeformed region
   Subgrain size = 1 mm
   $N_d = 2\times10^6/cm^2$ in the deformed region
   (excluding those formed into slip bands)

b) hot-forged sample
   $N_d = 1.2\times10^7/cm^2$
   Subgrains = 6.4 mm
   $\tilde{D}$ for the oxidation rate and hydroxyl diffusion when combined gives:
   $\tilde{D} = 96.8 \exp(-2.73\ eV/kt)\ cm^2/sec$

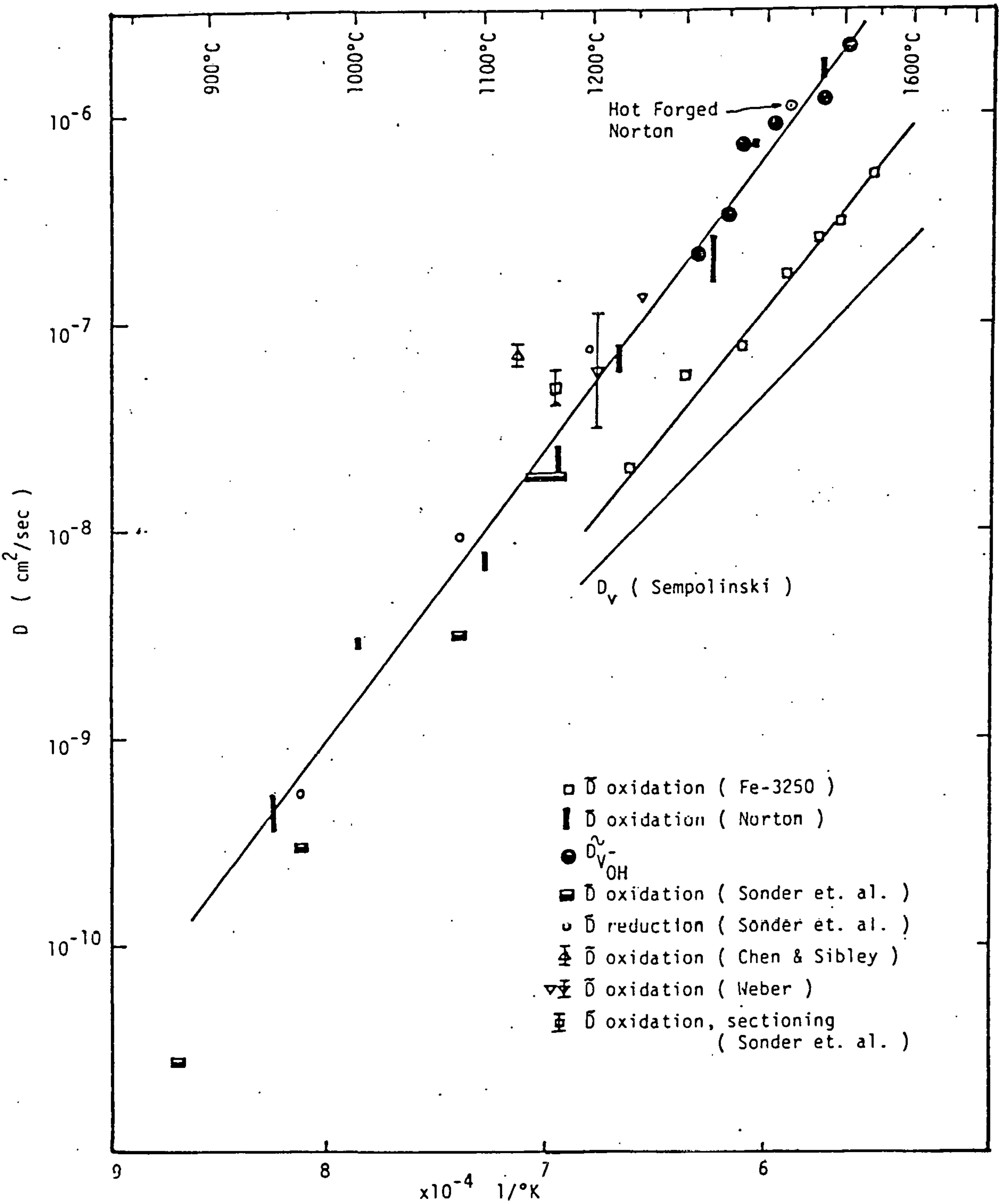

Figure 2.2.1 Oxidation rates of Norton crystals plotted against reciprocal temperature. Included are results of previous studies.

As shown in Figure 2.2.1, the effective diffusivity obtained from the Fe-3250 sample was about two to three times faster than the cation vacancy diffusivity D_v obtained by Kingery and Sempolinski (D. Sempolinski and W. D. Kingery). The effective diffusivity obtained from the undoped Norton crystals was about 10 to 20 times faster than the D_v.

The oxidation of Fe ions involves the introduction of cation vacancies into the bulk of the crystal. If the redox kinetics is controlled by the bulk diffusion of cation vacancies to and from the crystal surfaces, then, the effective diffusivity $\tilde{D} = 3D_v\overline{t_e}$, where $\overline{t_e}$ is the average electronic transference number. In semi-conductors $\overline{t_e} = 1$, therefore, $\tilde{D} = 3D_v$.

In MgO, which is a mixed conductor, $\overline{t_e}$ can be obtained from electrical conductivity measurements. The values of $\overline{t_e}$ can be obtained from Kingery and Sempolinski's conductivity data. The data for the Fe-3250 samples are analyzed by comparing the measured effective diffusivity and the calculated diffusivities and are presented in Figure 2.2.2. The fact that our data lie between D_v and $3D_v$ and that the experimental activation energy of 2.52 eV is in good agreement with the 2.72 eV of the calculated value of $3D_v$Fe, indicates that the redox kinetics of Fe ions in Fe-3250 sample is controlled by the bulk diffusion of cation vacancies to and from the crystal surfaces.

Now we have to explain the anomalously rapid redox kinetics observed in the undoped Norton crystals. The outstanding features of this anomalously rapid kinetics are summarized below:

(1) The redox rate is not controlled by D_{Fe}, D_o or D_v to and from the crystal surfaces.
(2) This rapid kinetics is not observed in the doped Fe-3250 samples.
(3) This rapid kinetics is <u>not</u> influenced by further increase in dislocation density.
(4) This redox rate was found to be identical to the effective diffusivity of OH^- ions.
(5) Since the redox rates were obtained from crystals free of OH^- impurities, the redox kinetics and the removal of OH^- ions seemed to be independent of each other.

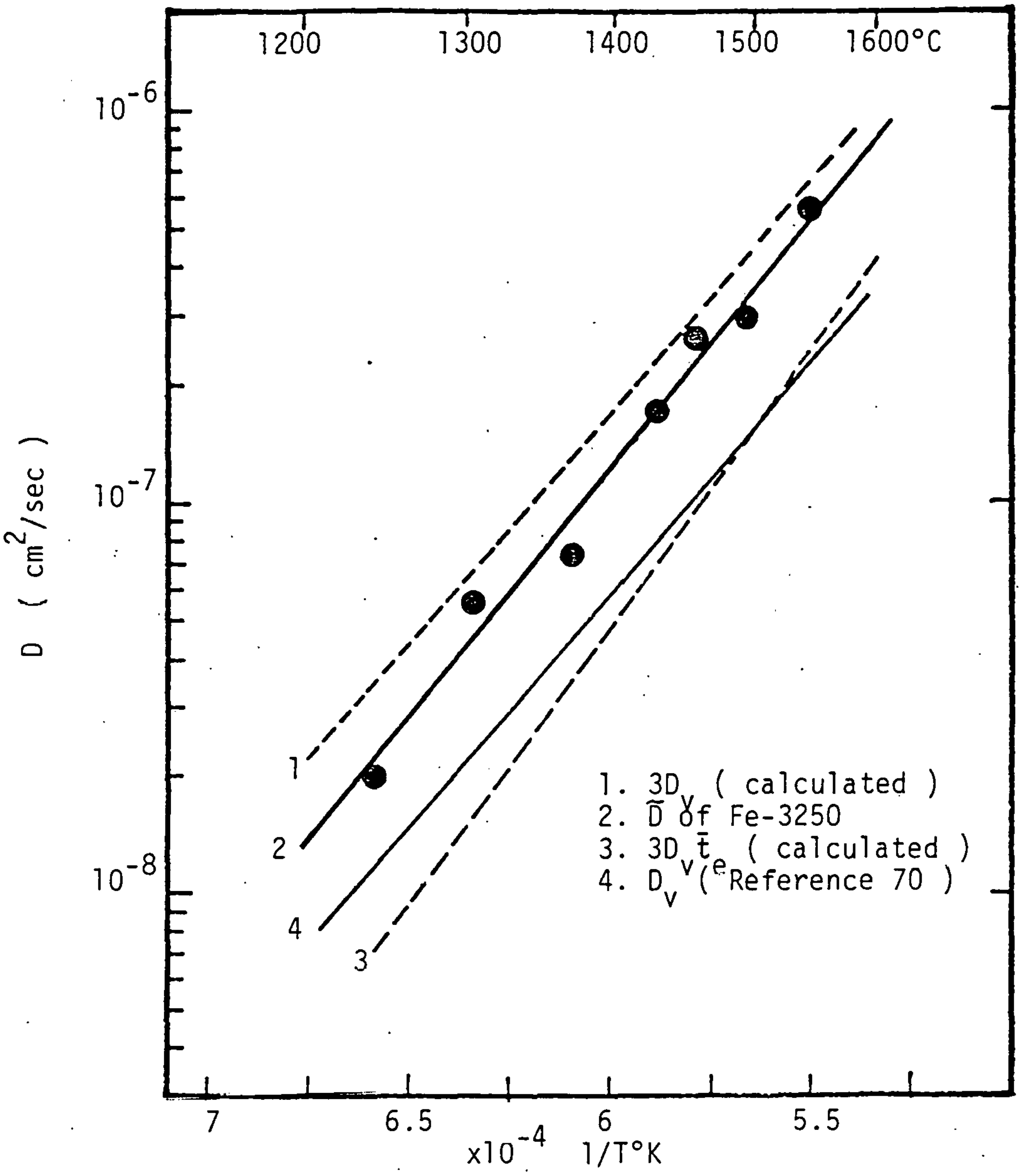

Figure 2.2.2 Experimental & Calculated Oxidation Rates for Fe-3250 Sample.

We want to propose a model to explain this anomalous kinetics. In this model, there is diffusion of oxygen down the dislocation pipe. The oxygen is incorporated into the lattice on reaching a jog. To continue this process, a magnesium ion has to move to the jog. This means that there is a two-step relaxation process - there is oxygen relaxation in the dislocation pipe and there is cation vacancy relaxation in the bulk between the dislocation pipes. A basic assumption made in this model is that the concentration of the diffusant in the dislocation pipe is large; therefore, the reaction at the jog does not perturb the concentration profile of the diffusant. This is analogous to the Whipple model in grain boundary diffusion.

The defect relaxation process betewen the very closely spaced dislocations only requires a few seconds. Therefore, the whole redox kinetics is controlled by the diffusion of oxygen in the dislocation pipes. This explains why further increase in dislocation density does not result in any enhancement of the oxidation kinetics. Although the model can explain one aspect of this anomalous kinetics, it involves a radical assumption that the lateral diffusion does not perturb the diffusion in the dislocation pipe. This requires either a very large concentration of the diffusant in the pipes or a large dislocation core. These have not been substantiated by any other experimental observations.

2.3 Hot Stage SEM Study of Microstructure Development

Personnel: E. Giraldez and W. D. Kingery

The sintering of powder compacts is an important step in the production of metallic and ceramic materials. During the sintering process, mass transport occurs when the material is heated to a temperature below the melting point. The compact shrinks, grain size changes and the pore volume resulting from the initial misfit of the powder is eliminated. Understanding the process taking place during the microstructural evolution of powder compacts is of importance both for commercial applications and to have a better understanding of the material itself.

A hot stage has been constructed to be used in conjunction with an ISI

Super II Scanning Electron Microscope. The stage consists of a heater, power source, radiation shields, platinum crucible and a R-type thermocouple. The heater is a tungsten wire wrapped around a high density aluminum oxide tube .32 inches in length and .25 inches I.D. Molybdenum foil is used as shielding material. It is placed around, below and on top of the heater. The top radiation shields have a hole so the primary beam can enter, and the secondary electrons can exit. By varying the size of the opening we can control the amount of heat liberated into the specimen chamber. The power comes from a ripple free D.C. power supply. The hot stage is capable of achieving a temperature of 1600°C in a couple of minutes. Magnification can be varied between 10x and 5000x. Low magnifications allow for statistical analysis of shrinkage, and at high magnifications, changes in morphology can be observed. Because of its high secondary electron coefficient at low accelerating voltages, magnesium oxide will be the primary material investigated. Even though a low accelerating potential is used to eliminate charging, the resolution is ten times that of an optical microscope.

Mass transport mechanisms responsible for the early stages of MgO sintering, which are dominated by surface diffusion phenomena, will be studied from direct observations of microstructure changes in MgO powder compacts and their dependence on time, temperature, composition, reactivity, source and atmosphere.

2.4 Oxygen Diffusion in Single Crystal MgO

Personnel: A. F. Henriksen and W. D. Kingery

The diffusion of cations - including the self diffusion of Mg in MgO has been extensively researched. Not so with the diffusion of anions. Thus, the diffusion behavior of oxygen in the MgO lattice has only been sparsely reported. From the present data it is generally agreed upon that the diffusivity of oxygen is about two orders of magnitude slower than that of Mg at a given temperature. But there seems to be some controversy with respect to the mechanism of diffusion of the oxygen. Also, due to the fact that no suitable radioactive oxygen isotope exists, radio tracer experiments are impossible; so, until now, most data have been derived from indirect methods, like gas-exchange experiments.

Thus, Oishi and Kingery determined the diffusivity of oxygen in single crystal MgO to be 2.5×10^{-6} exp (-62,400/RT) cm^2/sec (Y. Oishi and W. D. Kingery, J. Chem. Phys., 33, 905 [1960]). Using the same technique on sintered polycrystalline samples of MgO, Hashimoto and Hama (H. Hashimoto and M. Hama, J. Appl. Phys., 43, 4828 [1972]) found a value for $D_{ox} = 4.5 \times 10^{-7}$ exp (-60,200/RT) cm^2/sec. They noted that their data agreed with those of Oishi and Kingery. Therefore, they concluded that the oxygen diffusion in the boundaries was much faster than the bulk diffusivity. Later, experiments with oxygen diffusion in Li-doped, polycrystalline MgO showed a two orders of magnitude increase in the diffusivity compared to "pure" MgO in the range 1090-1420°C, resulting mainly from a decrease in activation energy from 60.2 kcal/mole to 44.4 kcal/mole (S. Shirasaki, H. Yamamura, M. Hama and H. Hashimoto, Japan J. Appl. Phys., 12, 1654 [1973]). It was concluded that the introduction of Li in the MgO lattice produced oxygen vacancies, thus facilitating oxygen mobility. The only direct-observation study on oxygen mobility was made by Narayan and Washburn (J. Narayan and J. Washburn, Acta Met., 21, 533 [1973]). By observing the rate of dislocation loop shrinkage with TEM, it was concluded that the oxygen diffusivity was $1.37 \pm 0.26 \times 10^{-2}$ exp (-110,000±4,200/RT) cm^2/sec. The activation energy of 62.4 kcal/mole was attributed to represent pipe diffusion.

In order to elucidate the existing discrepancies, it was decided to perform oxygen diffusion measurements on single crystal MgO using a SIMS with a sputtering attachment as in the work by Reed and Wuensch (D. J. Reed and B. J. Wuensch, J. Amer. Ceram. Soc., 63, 88 [1980]). One of the advantages of using a SIMS is that it is not necessary to have available a radioactive isotope. One can measure the concentration profile of the stable isotope, O^{18}. Also, it is possible to measure very small diffusion profiles extending only 3000-5000 Å into the bulk.

The experimental set-up was as follows: To determine whether the anion vacancy concentration has any influence on the diffusivity of the oxygen, three single crystals of MgO were doped with different amounts of Sc (500 ppm, 1500 ppm, and 5000 ppm) and homogenized. As it has been determined that Li_2O

as a dopant evaporates during heat-treatment, it was decided to affect the oxygen vacancy concentration through the introduction of Sc, instead. To determine the effect of dislocations, a sample of MgO which had been hot-pressed to 40% deformation was used as the fourth sample. A fifth sample of pure ORNL MgO (all material was ORNL MgO) was also included for reasons of comparison. All samples were treated exactly the same and simultaneously in the subsequent procedures. They were polished on one side to a ¼ micron finish and subsequently chemically polished with hot phosphoric acid to remove about 50 microns of damaged surface layer. The crystals were masked on one half, and on the other half were deposited about 1000 Å of 99.99% Mg-metal by evaporation. The crystals were then immediately transferred to a closed system containing enriched O^{18} gas at 200 torr and heated to 500°C for 45 mins. This procedure transformed the deposited Mg-layer into a MgO^{18}-layer. To avoid O^{16}/O^{18} exchange in the following diffusion anneal, the crystals were covered with a 0.35 micron thick layer of Pt by sputtering. The diffusion anneal was performed at 3×10^{-5} torr @ 1420°C for 11½ hrs and 1375°C for 9½ hrs. The drop in temperature during the anneal was unfortunate and a result of a power decrease during the experiment.

Presently, the samples are being analyzed by SIMS at the University of Illinois.

2.5 Boron Diffusion in Silicon Carbide

Personnel: K. Kijima and W. D. Kingery

Boron doping of silicon carbide is important for both high temperature ceramics and electronic materials. Boron and carbon are very effective additives for silicon carbide sintering. Also, boron is a typical dopant for making p-type silicon carbide semiconductors.

^{11}B was ion implanted in the basal surface of SiC single crystals using a beam energy of 50 kV. The distribution of the boron in SiC crystals, as implanted, was investigated by Auger Electron Spectroscopy (A.E.S.). Boron depth profiles in SiC samples showed Gaussian distributions. This was in agreement with ion range theory. A.E.S. measurements showed no detectable channeling and knock-on effects for the samples.

These samples were annealed at 1350°C, 1500°C, and 1600°C in vacuum of 2×10^{-6} torr. Boron depth profiles for annealed samples measured by A.E.S. showed Gaussian distributions with larger standard deviation than that of implanted samples. This spread is considered to be a result of boron diffusion during thermal annealing.

Diffusion coefficients of boron impurities in SiC were calculated from the depth profile data before and after annealing, using the following equation:

$$n(x,t) = \frac{n(R,0)\ x\sqrt{2R_s^2}}{\sqrt{2R_s^2 + 4Dt}} \exp\left[-(x - R)^2/(2R_s^2 + 4Dt)\right] \quad ,$$

where

$n(x,t)$ = the concentration at x and t
x = the distance from the surface
t = a diffusion time
D = a diffusion constant
R = ion range of implantation
R_s = standard deviation in a Gaussian
$n(R,0)$ = a peak concentration at $t = 0$.

A diffusion constant of $(5.45\pm0.49)\times10^{-17}$ cm^2/sec was obtained for boron diffusion in the <0001> direction of silicon carbide from isothermal experiments at 1350°C. The value falls within a difference of one order of magnitude from the extraporated values ($D_T = 1.15\times10^{-16}$ cm^2/sec for T section and $D_I = 5.30\times10^{-16}$ cm^2/sec for I section) of Vodakov (Y. A. Vodakov and E. M. Mokhov, in "Silicon Carbide-1973", ed. by R. C. Marshall, J. W. Faust, Jr., and C. E. Ryan, University of South Carolina Press, Columbia, SC, 1974, p. 508).

They used p-n junction and electrical conductivity methods to obtain the diffusion parameters. The use of the electrical conductivity method presents difficulties due to high activation energies of the impurities (which are only partially ionized at room temperature) and to the presence of surface inversion layers with an energy barrier higher than 1 eV. Their results showed that diffusion profiled depended upon the surface concentration. With small C_s^B ($\leq 3 \times 10^{18}$ cm^{-3}) the distribution is of simple form, but with increasing C_s^B the character of the diffusion profile becomes more complicated.

2.6 Quenching of Lattice Defects in KCl

Personnel: T.R. Gattuso and R.L. Coble

Our model for the process of lattice defect trapping in alkali halide crystals by means of rapid cooling from high temperature has been extended to include the effects of impurities. The predominant intrinsic point defects in alkali halide crystals are separated Schottky defects and neutral vacancy pairs. Divalent cation impurities are present in even the purest available material, however, such that all "pure" crystals undergo transitions from intrinsic to extrinsic during cooling. We have modeled the evolution of the point defect population in KCl crystals of general purity during rapid cooling allowing migration of excess anion vacancies, excess cation vacancies and excess vacancy pairs to dislocation sinks. Interaction of free vacancies to form vacancy pairs and interaction of free cation vacancies (V) with free cation impurities (I) to form I-V complexes has been allowed as well.

For the general case a set of four coupled differential equations has been derived describing the net rate of excess defect production:

$$\frac{dP_x}{dt} = \frac{dP_e}{dt} - \dot{P}_{loss} + \Phi_P$$

$$\frac{dn_x}{dt} = - \frac{dm_e}{dt} - \dot{n}_{loss} - \Phi_{P,c} - \Phi_I$$

$$\frac{dm_x}{dt} = - \frac{dm_e}{dt} - \dot{n}_{loss} - \Phi_{P,a}$$

$$\frac{dI_x}{dt} = \Phi_I$$

In these equations, the symbols P, n, m and I represent the mole fractions of vacancy pairs, cation vacancies, anion vacancies and I-V complexes, respectively. The subscript e denotes equilibrium concentration while the subscript x denotes concentrations in excess of the equilibrium values. Since only thermal defects are of interest the equality of n_e and m_e has been emphasized, as well as the equality of anion vacancy and cation vacancy loss rates that is required by charge neutrality. The loss rates are all of the form

$$\dot{C}_{loss} = \frac{2\pi C_x D_c}{R^2 [\ln(R/b) - 3/5]}$$

where 2R is the sink spacing, b is a capture radius, C_x is the excess concentration of the species of interest and D_c is the appropriate diffusivity. The vacancy pair diffusivity is given by

$$D_p = \frac{4a^2 W_1 W_2}{3(W_1 + W_2)}$$

where a is the anion-cation separation; W_1 and W_2 are the frequencies of anion and cation jumps into the pair. The loss rate for free vacancies is determined by an effective diffusivity given by

$$D_{eff} = \frac{D_n D_m [m + n(1 + \nabla I_x / \nabla n_x)]}{nD_n + mD_m} .$$

In this expression n and m represent total concentrations, D_n and D_m are cation vacancy and anion vacancy diffusivities, respectively, and $\nabla I_x / \nabla n_x$ is the ratio of the gradients of I-V complexes and free cation vacancies.

In equations 1-4 the terms in Φ are rates at which defects are lost or gained as a result of association reactions. Since no lattice sites are created or destroyed by means of the interactions the Φ terms can be eliminated by algebraic combinations of equations 1-4. Solution of the resultant differential equation requires knowledge of the partitioning of the defects in the supersaturated crystal. We have solved equations 1-4 for the case where the association reactions

$$V_K' + V_{Cl} \longrightarrow (V_K'V_{Cl})^*$$

$$M_K^{\cdot} + V_K' \longrightarrow (M_K^{\cdot}V_K')^*,$$

where M is a divalent cation impurity, remain in local equilibrium. Independent calculations of association reaction rates show that this is a good assumption over the temperature range where defect losses are important. We find that the essential features of the solution are similar to those for the case of ideal purity. Vacancy pairs dominate the defect structure in the supersaturated crystal and the retained defect fraction becomes less sensitive to the quench temperature as the cooling rate or sink spacing decrease. The effect of impurity additions depends upon cooling rate and sink spacing. At high cooling rates or large sink spacings defect losses are unimportant. The retained defect fraction decreases with increase impurity levels because of the reduction in the number of thermal defects. At lower cooling rates or smaller sink spacings the effect is reversed. In this case defect losses are reduced by divalent cation additions because of the reduction of the effective diffusion coefficient for free vacancies.

Experimental confirmation of the model remains unavailable. The early attempts to observe excess vacancy concentrations in quenched crystals by means of microdensitometry were thwarted by observations of anomalous density increases. In the early work samples were heat treated in a platinum basket. Information on the decomposition of K_2PtCl_6 suggests that reaction of the Pt and KCl was occurring above T_{eu} for the KCl-K_2PtCl_6 system. During slow cooling the reaction product decomposes, while during rapid cooling it does not, and the density difference between slowly cooled and rapidly cooling crystals, as well as the observed recoverability of the density in rapidly cooled crystals, can be accounted for.

In later work with crystals heat treated in contact only with pure KCl and quenched into isopropanol no density change could be observed. Photoelastic examination revealed that the crystals had plastically deformed because of thermal stresses during quenching. Calculations show that the retained defect fraction falls very rapidly with increased dislocation density suggesting that annihilation of excess lattice defects at the newly generated dislocations occurred during quenching. Photoelastic examination of crystals quenched into saturated brine according to the procedure of Pellegrini and Pelsmaekers (J. Chem. Phys. 51, 5190 (1968)) showed extensive deformation and it is believed that the density decreases reported by these authors resulted from debris produced by dislocation interactions or by microcracks at slip band intersections.

The most recent experimental attempts have involved encapsulating sample crystals in a quartz tube and quenching by directing a high velocity gas stream over the tube. Cooling rates between 100 and 150°/sec could be achieved in this way and photoelastic examination of quenched crystals revealed no obvious deformation. The density data for these quenches was very erratic. Density changes in the anticipated range were occasionally observed, however, changes both larger than anticipated and smaller than the resolution of the densitometer were also observed as well as changes of the wrong sign. Reasons for this behavior remain obscure.

3.0 Defect Structures, Defect Interactions, Grain Boundaries and Surfaces

3.1 Grain Boundary Phenomena in Electronic Ceramics

Personnel: W. D. Kingery

A review and analysis of grain boundary phenomena has been prepared and presented at an international symposium organized by the American Ceramic Society. It will be published in full by the Ceramic Society.

In summary, grain boundaries in electronic ceramics are found to be paths of high diffusion for oxygen and for other constituents that can have a strong influence on processing. Control of oxygen pressure and the cooling and heating cycles used in sample preparation is essential. Grain boundaries generally have an electrical charge associated with ionic concentrations or electronic surface states and an associated space charge layer that depends in a complex way on both the ionic and the electronic defect structure of the material. Since these characteristics depend on both temperature and composition, and since precipitation, segregation and oxidation of boundaries during firing and cooling are common, we have to consider a complex set of phenomena in which many variables, including the basic crystallographic structure of the boundary, are only comprehended to a first level of approximation.

At the same time, boundary phenomena are critical to the use of ceramic materials as insulators, conductors, resistors, varistors, positive temperature coefficient resistors and barrier layer capacitors, and strongly affect the useful characteristics and properties of ferromagnetic and ferroelectric ceramics as well.

Obviously, the study of grain boundary structures and properties in electronic ceramics is a field in which there are both great needs for more extensive understanding and great opportunities for further developments.

3.2 The Electrical Properties of Grain Boundaries in MgO

Personnel: L. Dolhert, J. Gambino and W. D. Kingery

Electrical conductivity studies are in progress on sintered MgO polycrystals and deformed MgO single crystals in order to understand the influence of grain boundaries on conduction in MgO. In previous work, the electrical properties of single crystal MgO have been characterized well enough that a study of the more complex electrical behavior of grain boundaries can be more easily interpreted.

The sintered MgO polycrystals are prepared by co-precipitation of the appropriate hydroxides, followed by calcination, and then sintering at 1400°C for 1 hour.

The deformed single crystals are prepared by hot pressing in vacuum at 1400°C. Dislocations are formed which line up to form low angle grain boundaries. Samples of 15% and 30% strains will be compared to previously tested unstrained crystals. The deformed crystals are "pure" Norton (∿ 100 ppm Fe) and pure Oak Ridge MgO.

The sintered MgO specimens are doped with either Fe or Sc so that only one solute controls the defect structure. From the previous work with single crystals, the ionic charge carrier is believed to be V''_{Mg} which is generated when trivalent solutes are introduced into the MgO. By using the same doping levels and the same DC conductivity and transference number measurements as in the single crystal study, any change in the electrical properties of the present MgO specimens can be attributed to the presence of grain boundaries. Measurements are performed under conditions where ionic conduction probably dominates at temperatures of 1100°C to 1400°C and oxygen pressures of 10^{-4} to 10^{-6} atm.

Preliminary measurements indicate there is enhanced ionic conductivity in specimens with grain boundaries.

3.3 Laser-Heated High-Temperature EPR Spectroscopy

Personnel: T. A. Yager and W. D. Kingery

A CO_2 laser-heated EPR system capable of temperatures above 1200°C has been developed in which only the sample is heated. Thus, a cylindrical cavity is used which permits rotation of the magnet around the sample. Rapid temperature changes are dependent only upon the thermal properties of the sample itself. A schematic diagram of the laser-heated EPR system is shown in Figure 3.3.1. A Varian E-9 EPR spectrometer operating in the X-band with a Varian E-233 rotating cylindrical cavity operating in the TE_{011} mode was employed. The sample within the cavity was heated by an Apollo model 500 50-W CO_2 laser. Proper beam alignment was crucial to minimize thermal gradients and was achieved using a small He-Ne laser emitting a visible beam. A temporary reflector was placed in the path of the CO_2 laser beam and used to align the He-Ne beam so that it passed through holes which had been burned in two plastic alignment sheets. Both lasers were then aligned to each other in order that two gold-plated reflectors could be precisely positioned. With the temporary reflector removed, the CO_2 laser was then used to uniformly heat the sample.

A Pt-Pt/13% Rh thermocouple bead was imbedded within the sample. The 5 mil leads passed to a 0°C reference junction, and the emf was continuously monitored by a digital volt meter from which the sample temperature was derived. The emf also led to two isolation amplifiers. One of these was linked to a proportional temperature controller in order to modulate the power of the CO_2 laser. With this feedback system the sample temperature was controlled to within ±1°C from room temperature to 1000°C and within ±3°C from 1000 to over 1200°C. The second isolation amplifier led to a recording oscilloscope in order to follow rapid heating or cooling rates. Both amplifiers were adapted with a low by-pass 60 Hz filter to improve their operational performance.

The sample holder was constructed primarily of commercial grade fused SiO_2 and was of double-wall construction to allow high-velocity cooling air to pass within the jacket. The sample must be a material which absorbs 10.6 μm

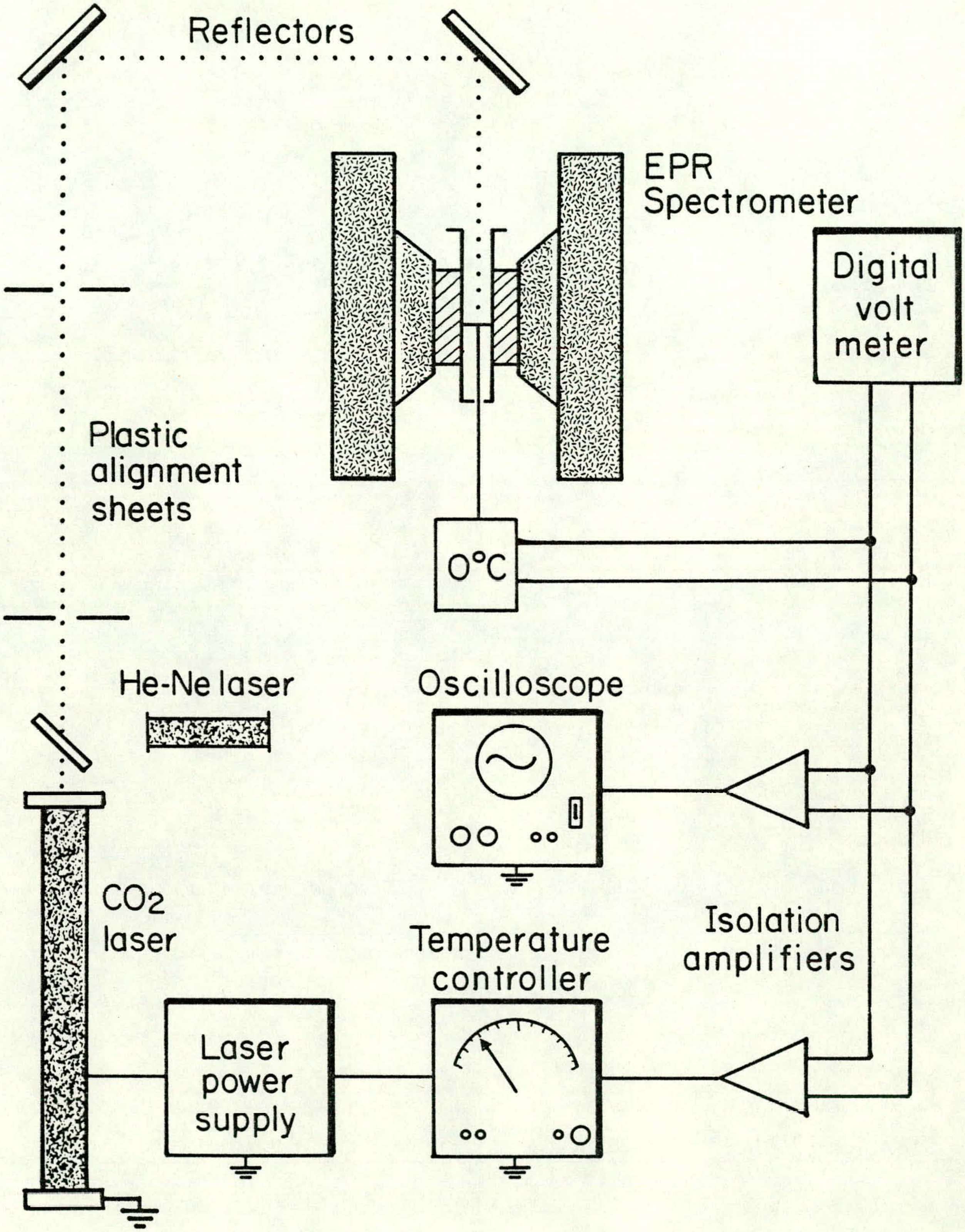

Figure 3.3.1   High-temperature EPR apparatus.

radiation with minimal reflectivity; otherwise, a susceptor is required. The sample (with dimensions of 4.8×4.8×1 mm) was positioned on a fused silica capillary tube and held in place by a 10 mil platinum wire which passed through the center of the sample. One of the thermocouple leads passed through the center of the capillary tube while the other was attached to the outside. The capillary tube was held in place by a platinum foil covered cork. An additional port was present for a liquid nitrogen quench. The sample was quenched using a series of solonoids which turned off the laser and blew liquid nitrogen into the sample tube. The measured cooling rate within the spectrometer was found to be comparable to the rate measured by dropping a sample at 1200°C into a container of liquid nitrogen, while the heating rate was limited only by the thermal shock resistance of the sample.

The room temperature and 1200°C EPR spectra of single-crystal MgO containing 4300 ppm Fe are shown in Figure 3.3.2. The spectral lines in Figure 3.3.2 have been labeled O, T and R, attributed to Fe^{3+} in octahedral, tetragonal and orthorhombic electric fields.

The particular advantage of this system is that only the sample is heated. This allows adequate temperature uniformity and control, rapid temperature change, rotation of the magnet around the sample, and a controlled atmosphere. These capabilities are useful for studying the characteristics and interactions of defects giving rise to EPR spectra.

3.4 The Equilibrium Defect Structure of Iron-Doped MgO in the Range 600 - 1200°C

Personnel: T. A. Yager and W. D. Kingery

Trivalent iron forms substitutional solid solutions in MgO with its effective positive charge compensated by the effective negatively charged magnesium ion vacancies. Using Kröger-Vink notation, the solution of trivalent iron in MgO can be written

$$Fe_2O_3 \xrightarrow{MgO} 2Fe^{\cdot}_{Mg} + V''_{Mg} + 3O^{x}_{O} \ .$$

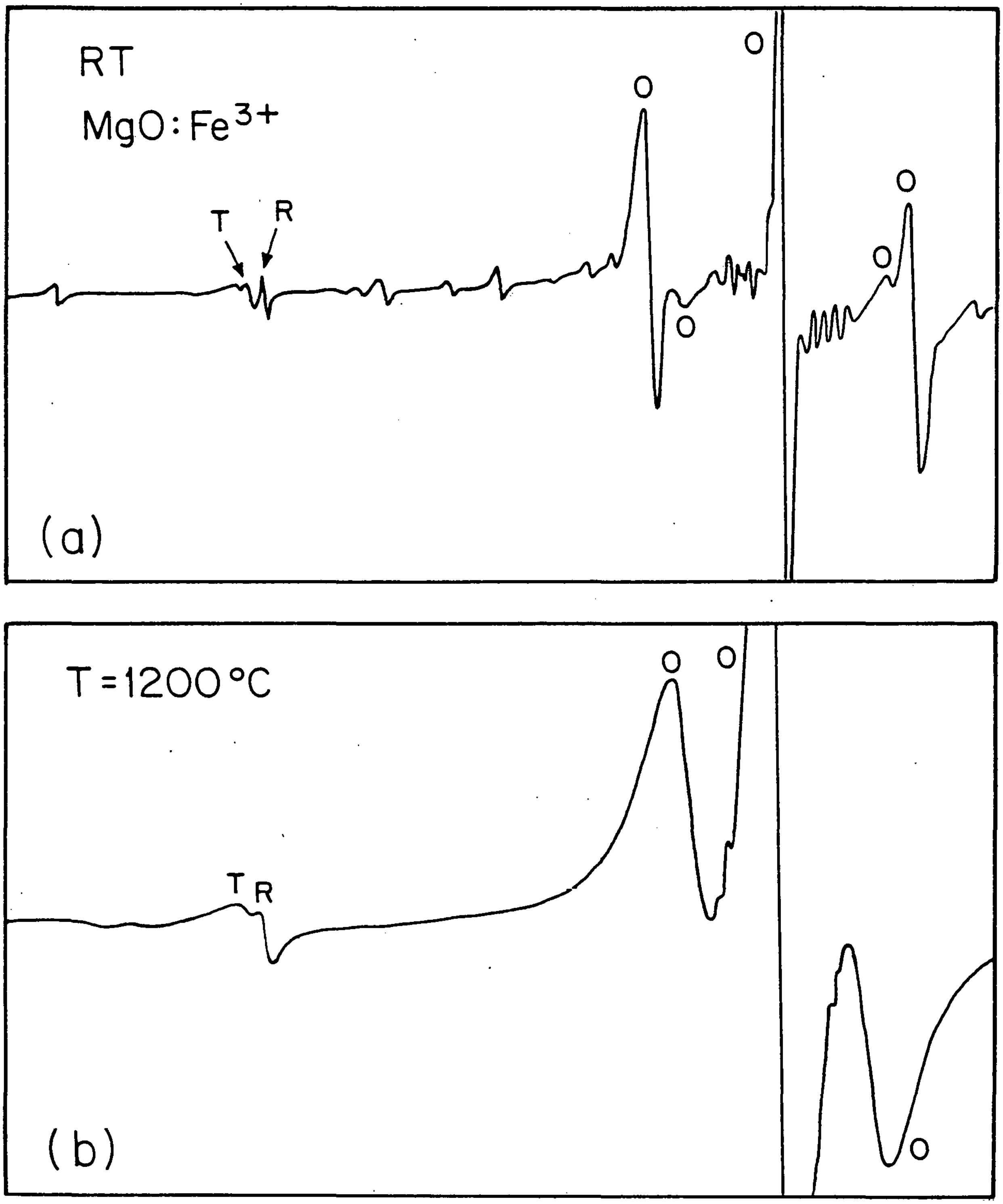

Figure 3.3.2 (a) Room temperature and (b) 1200°C EPR spectra of single crystal MgO containing 4300 ppm Fe.

Coulombic attraction between $Fe_{Mg}^{\bullet}$ and V_{Mg}'' results in association to form a negatively charged dimer according to the equilibrium reaction

$$Fe_{Mg}^{\bullet} + V_{Mg}'' = (Fe_{Mg}^{\bullet}-V_{Mg}'')' \quad .$$

Depending on the location of the vacancy, a dimer may be oriented in either the <100> (termed D<100>) or the <110> (termed D<110>) crystallographic direction. Additional association may occur due to the coulombic attraction of a dimer and another iron to form a neutral trimer

$$(Fe_{Mg}^{\bullet}-V_{Mg}'')' + Fe_{Mg}^{\bullet} = (Fe_{Mg}^{\bullet}-V_{Mg}''-Fe_{Mg}^{\bullet})^{x} \quad .$$

Two linear trimers exist along <100> or <110> directions, and several non-linear trimers may exist.

Phase separation occurs to form magnesioferrite spinel precipitates. This reaction may be written

$$Mg_{Mg}^{x} + 2Fe_{Mg}^{\bullet} + V_{Mg}'' + 4O_{o}^{x} = MgFe_2O_{4(ppt.)} \quad .$$

Since dimers and trimers are present during phase separation, the actual reaction process is some unknown combination of these equations.

Relaxation processes during a quench were found to be sufficiently rapid to cause association and clustering in the room temperature material. Thus, the defect structure of quenched MgO does not correspond to the equilibrium high temperature structure. The present study applies high temperature EPR spectroscopy to the analysis of the equilibrium defect structure of Fe^{3+}-doped MgO in the temperature range 600-1200°C. This technique eliminates the quench problem by permitting measurements in situ of several defect centers simultaneously. Additionally, the ability of EPR spectroscopy to detect low concentrations of ferrimagnetic precipitates has provided a means of extending phase equilibria measurements to low solute level samples.

High-temperature EPR spectroscopy with a CO_2 laser heat source was used to monitor defect concentrations at temperatures up to 1200°C with less than ±10°C thermal gradients across the sample.

On cooling to room temperature the EPR spectra was almost completely masked by a very broad peak centered near g=2. This peak has been previously reported and related to ferrimagnetic precipitate resonance. The broad peak was often accompanied by a deep orange coloration of the sample, both of which were removed by a short annealing period above 1000°C followed by quenching. That is, quenching was sufficiently rapid to prevent precipitation during the quench.

To confirm the identification of this broad resonance, the temperature dependence of the peak intensity was studied. The intensity was found to decay monotonically as the temperature increased and was completely absent at 210°C. This corresponded to the Curie temperature of 217°C for magnesioferrite particles precipitated from MgO containing approximately 1% Fe.

The EPR spectra of MgO containing 310-4300 ppm Fe at 600-1200°C show peaks corresponding to $Fe_{Mg}^{\bullet}-V_{Mg}''$ associates in the <100> direction, the <110> direction and an unassociated $Fe_{Mg}^{\bullet}$. Mass action relationships among these associates have been analyzed as a function of temperature and concentration. It was found necessary to include Debye-Hirchel corrections for an applicable quantitative analysis. With these corrections, good agreement with prior data for heats of solution and good constancy of equilibrium constants were found.

The quantitative data on equilibrium association, clustering, and phase separation are presented in Table 3.4.1. The column labeled -E/Fe refers to the total energy change per iron going from an isolated ion to an ion in the product. The energy per Fe increases monotonically with increasing size of the product. A difference of 0.55 eV exists between the energy change per Fe for the 3-cluster and the precipitate; therefore, several other species of metastable clusters could exist having energies between 1.36 and 1.91 eV/Fe.

The calculated curves show a good fit to the experimental data points above the phase separation temperature. Below this temperature, the calculated curve consistently lies below the experimental values. This indicates that single phase clusters are not dominant in the concentration range studied. On phase separation, metastable clusters, precipitates, and mobility limitations govern the reaction rather than equilibrium limitation.

Table 3.4.1

QUANTITATIVE EVALUATION OF THE DEFECT STRUCTURE OF $MgO:Fe^{3+}$ BELOW 1200°C

Reaction	A	-E(eV)	-E/Fe (eV)
$Fe_{Mg}^{\cdot} + V_{Mg}'' = D\langle 110\rangle$	0.6 to 1.7	0.85±0.05	0.85
$2D\langle 110\rangle + Fe_{Mg}^{\cdot} = \text{3-cluster}$	8×10^{-6} †	2.38	1.36
$Mg_{Mg}^{x} + 2Fe_{Mg}^{\cdot} + V_{Mg}'' + 4O_{o}^{x}$ $= MgFe_2O_4$ (ppt.)	$(5.86 \text{ to } 11.2)\times10^{-6}$	3.83±0.04	1.91

where $K_{eq} = A \exp -E/K_bT$

---

† Estimated value.

3.5 The Kinetics of Clustering Reactions in Iron-Doped MgO

Personnel: T. A. Yager and W. D. Kingery

Trivalent iron enters the MgO lattice substitutionally with its effective positive charge balanced by the negative magnesium vacancy. Using Kröger-Vink notation, the solution process consists of

$$Fe_2O_3 \xrightarrow{MgO} 2Fe^{\bullet}_{Mg} + V''_{Mg} + 3O^{x}_{o} \quad .$$

Coulombic attraction results in formation of $Fe^{\bullet}_{Mg}$-V''_{Mg} dimers, which may be oriented in either the <100> or <110> crystallographic direction. Additional association may occur to form a neutral trimer, consisting of two $Fe^{\bullet}_{Mg}$ associated with one V''_{Mg}. Two linear trimers along <100> or <110> directions and several non-linear trimers may occur.

During the process of phase separation, several intermediate defect clusters may form, as has been found in studies of defect clustering in alkali halide crystals doped with divalent impurities, where a two-stage third order kinetic decay was observed, attributed to the aggregation of three dimers to form a cluster, and the growth of higher order complexes. The third order kinetic decay was subsequently confirmed using EPR measurements and optical spectroscopy. Based on an analysis of the measured kinetics, the atomistics of defect clustering were evaluated and mechanisms for the process proposed.

No previous systematic studies of clustering kinetics have been reported for MgO containing trivalent impurities, although the association process at high temperatures has been investigated. The approach used in this study is the application of high-temperature EPR spectroscopy to the evaluation of relaxation phenomena in quenched single crystals of iron-doped MgO.

The Fe<110> peak has provided the most information about the kinetic reactions. Since only one vacancy jump transforms a D<110> dimer to a D<100> orientation, their concentrations are assumed to be in metastable equilibrium and proportional to each other. Therefore, the signal intensity of the Fe<110> peak serves to measure not only the concentration of the dimer oriented in the

<110> direction, but (with a different proportionality constant) the total dimer concentration as well.

During the isothermal anneals, Fe<110> was analyzed for the order of kinetic decay. The data did not fit either first or third order decay, but a plot of $1/I_{Fe<110>}$ versus time for the temperature range 400°C to 500°C is linear, indicating a second order reaction, i.e.,

$$\frac{dc}{dt} = -kc^2 \quad .$$

The second order decay of dimers implies the reaction of two dimers to form an initial cluster. Electrostatic repulsion of the negatively charged dimers makes a direct combination unlikely and suggests that a positively charged defect might be involved. Consider:

$$2 \text{ dimers} + Fe^{\bullet}_{Mg} = \text{3-cluster} \quad .$$

Since direct reaction would involve a three-body collision, a two-step process seems more likely, i.e.,

$$\text{dimer} + Fe^{\bullet}_{Mg} = \text{trimer}$$

$$\text{dimer} + \text{trimer} = \text{3-cluster} \quad .$$

This two-step process leads to second order kinetics so long as the first step is slower and the $Fe^{\bullet}_{Mg}$ and trimer species act as immobile traps for the mobile dimers. Similar kinetics are found for impurity pairing reactions in germanium.

The decay rate of the Fe<110> peak was also used to analyze the diffusional properties of the dimer. For a diffusion-limited reaction, the kinetic decay constant can be written

$$k \simeq \frac{k_o}{T} \exp \frac{-Q}{kT}$$

where k_o is a constant dependent on the initial concentration of all reacting species.

In low dopant level crystals of iron-doped MgO quenched from 1100°C into liquid nitrogen, the second order concentration decay of $Fe^{\cdot}_{Mg}$-V''_{Mg} dimers is in accord with a process consisting of aggregation of two dimers and an unassociated iron to form a 3-cluster similar to reactions found in alkali halides doped with divalent cations. Interpretation of reaction kinetics according to this model permitted evaluation of the dimer diffusion coefficient and the equilibrium constant for 3-cluster formation. Relaxation during the quench was found to deplete the system of unassociated vacancies, leaving a room temperature supersaturation of unassociated $Fe^{\cdot}_{Mg}$ and dimers in equal concentrations.

3.6 Characterization of Grain Boundary Segregation in MgO

Personnel: Y. M. Chiang, A. F. Henriksen, W. D. Kingery and
D. Finello (Dept. of Mechanical Engineering, University
of Texas at Austin, Austin, Texas)

Recent studies have shown that solute segregation at interfaces in oxides is quite common indeed. In the present investigation we have used Auger electron spectroscopy (The AES analysis was carried out in the Mechanical Engineering Laboratory of the University of Texas at Austin.) concurrently with inert ion sputtering to determine more precisely the concentration profile of segregants at the boundary in MgO containing Sc and the impurities Ca and Si.

A polycrystalline MgO specimen was isostatically pressed from powder produced by a continuous flow hydroxide coprecipitation process which ensured uniform particle size and solute distribution. The concentration of Sc was determined to be 3000±300 cation ppm by atomic absorption analysis. The Ca and Si impurity levels were not analyzed; they are typically 100-200 ppm in such coprecipitated powders. The sample was heat-treated in air, first at 1600°C for 6 hours to attain solid solution and then at 1200°C for 165 hours to allow equilibrium segregation of solutes to the grain boundary. Following heat treatment the sample was rapidly cooled in air at a rate of ∿10°C per second.

A Sc-doped single-crystal calibration standard was also prepared in order to characterize the sputtering of Sc in the MgO matrix and to obtain the Auger sensitivities of these elements for later quantification of grain boundary segregation. This standard was prepared by embedding a flat crystal (10×10×0.55 mm) of high purity MgO (Oak Ridge National Laboratory, Oak Ridge, Tennessee) in a 9 to 1 powder mixture of 99.9 (R.E.O.) Sc_2O_3 and pure MgO. The assembly was isostatically pressed at 20,000 psi to ensure good contact between powder and crystal and then heat-treated at 1760°C in air for 3 hours to diffuse in the desired quantity of Sc. The powder shell was removed and the crystal was homogenized at 1760°C in air for 215 hours. Homogeneity of Sc was confirmed by heat-treating the crystal at 900°C for 165 hours to exsolve Sc_2O_3 second-phase precipitates, the uniform distribution of which was verified with SEM after cleaving the crystal and etching the cross-sections in 98% H_2SO_4. A segment of the crystal was then re-homogenized at 1670°C for 13 hours to be used as the standard. The Sc concentration was determined after AES analysis from accurate lattice parameter measurements, made using a Debye-Scherrer technique, to be 17,800±1900 cation ppm Sc.

For AES derivative spectra and sputter-profiling analyses, both specimen and standard were fractured in high vacuum (less than 10^{-9} Torr) immediately prior to analysis, in order to provide a clean surface, free from externally adsorbed impurities. A flat, well-exposed grain boundary of about 30 μm width on the fracture face of the polycrystalline specimen was selected for analysis, here shown in Figure 3.6.1. The AES electron beam was focused to 5 μm upon this site, centered within the much larger area (∿1 mm) sputtered by the ion beam. On the calibration standard, a planar {100} fracture face was chosen for similar analysis. In order to determine the rate of sputtering, a polished single crystal of MgO was masked and sputtered for 30 hours under the same experimental conditions as the specimens, and the step height between masked and sputtered portions measured with interferometry.

The sputter profile of the calibration standard showed little change in the Sc signal, indicating that neither preferential enrichment nor removal of Sc in the MgO matrix of a significant degree occurs upon sputtering. Consequently, Sc concentration changes observed in the sputter-profile of the grain boundary

Chiang, Henriksen, Kingery and Finello
Figure 3.6.1

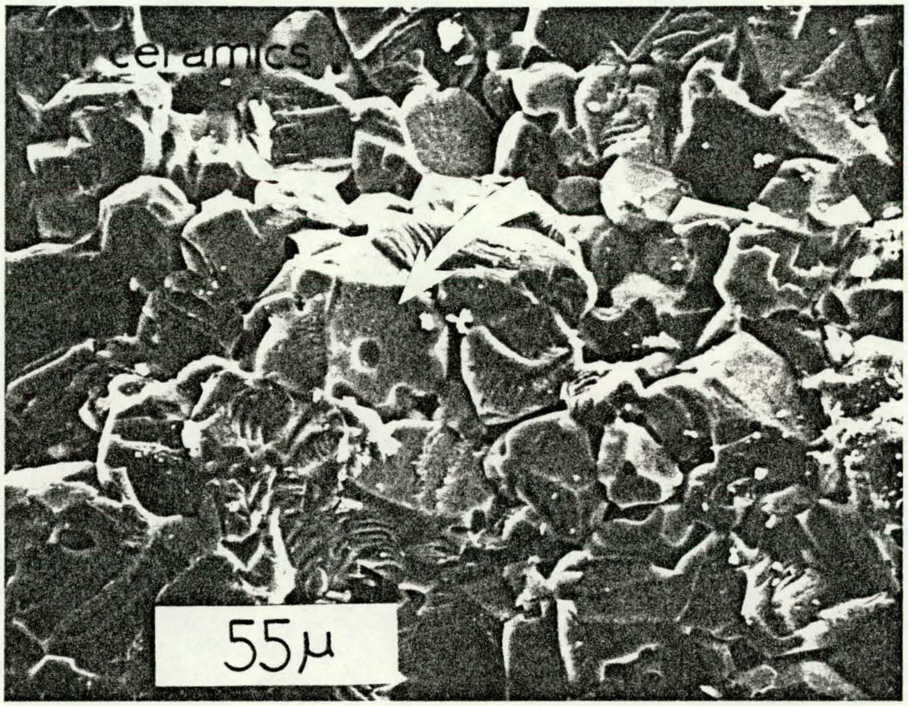

Figure 3.6.1 Fracture face of polycrystalline MgO specimen containing 3000 cation ppm Sc. The grain-boundary site of AES analysis is indicated by the arrow (450X).

may be considered real and not artifacts of the sputtering process.

The sputter-profile of the grain boundary site is shown in Figure 3.6.2, where the change in the peak-height ratios Si/Mg, Ca/Mg and Sc/Mg are monitored with depth of penetration. The Si and Ca signals decrease to background levels in less than 10 Å; the profiles are as expected for partial monolayer adsorption at the boundary and correspond closely to what has been observed in metals. The Sc segregation profile, however, in which the width of segregation extends out to about 25 Å, clearly indicates a different type of behavior.

Boundary segregation of solutes can result from strain effects. When the solute atom differs in size from the solvent atom for which it substitutes, accommodation of the solute atom at boundaries or other lattice imperfections will result in a lowering of the expended strain energy as compared to accommodation in the bulk.

When considering aliovalent solutes, however, the existence of a boundary charge can also cause segregation of species of the opposite sign adjacent to the boundary. The result is the formation of a space-charge segregation layer, which at equilibrium completely balances the boundary charge. In simple ionic solids the energy needed to create a cation vacancy is generally assumed to be less than that for an anion vacancy, and thus, for a completely pure material, the expected boundary charge is positive and the space charge is negative. In MgO, however, the energy for intrinsic vacancy formation is sufficiently large (Schottky energy about 7 eV) that even in so-called "pure" material, the concentration of thermally generated vacancies is small compared to the concentration of cation vacancies generated by aliovalent impurities in order to maintain charge neutrality in the bulk. As a consequence of the defect equilibrium, the respective signs of the boundary and space charge are reversed.

In the case of Sc^{3+} in the MgO lattice, strain effects are unlikely to be a major cause of segregation, as the ionic radius of Sc^{3+} (0.73 Å) is very close to that of Mg^{2+} (0.72 Å). We thus attribute the increased concentration of Sc adjacent to the boundary to a positive space charge balancing the negative boundary charge, where the segregating defect species is unassociated Sc with an effective +1 charge.

Chiang, Henriksen, Kingery and Finello
Figure 3.6.2

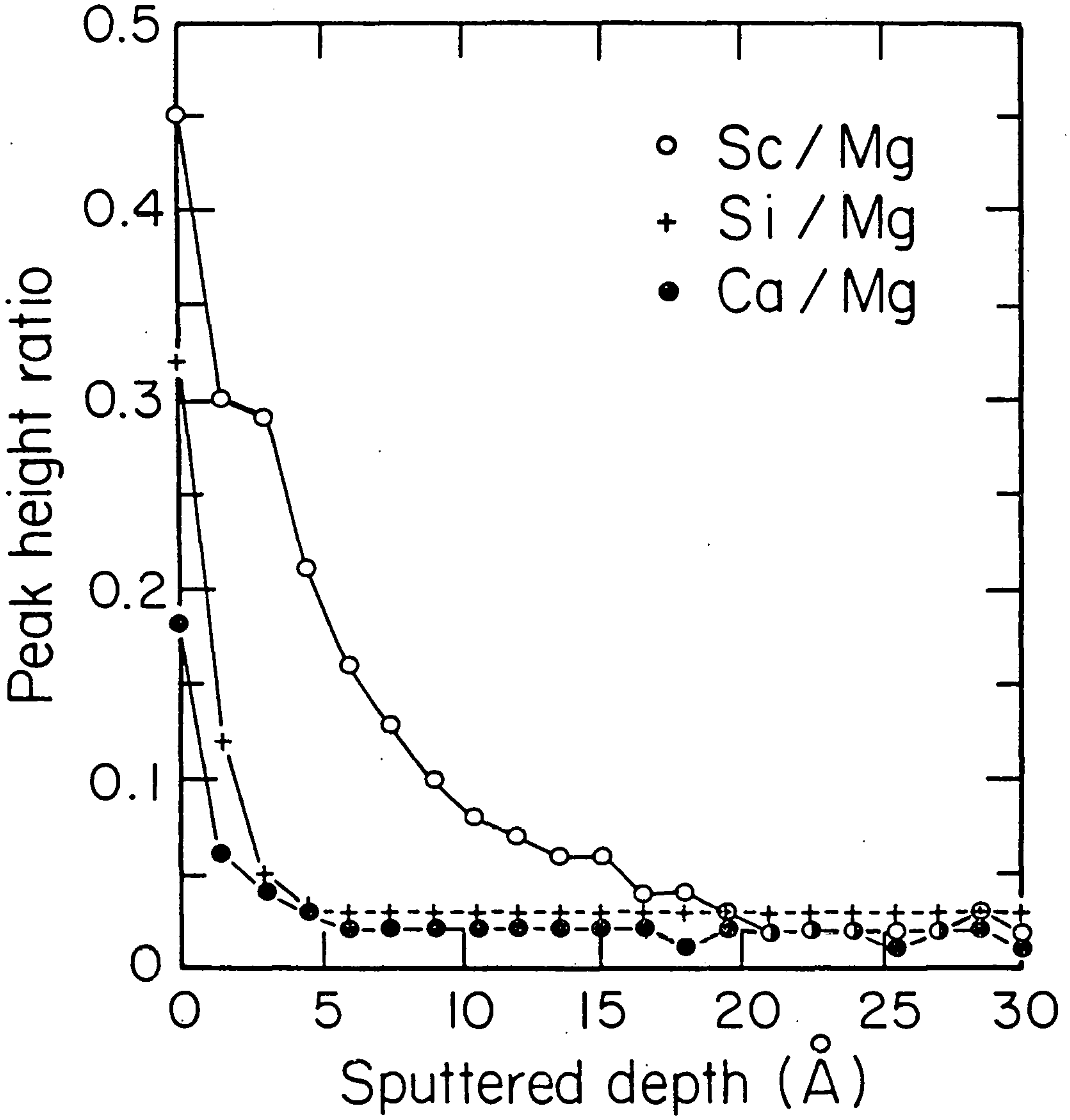

Figure 3.6.2 The ratios Sc/Mg, Si/Mg and Ca/Mg in sputter-profile of grain-boundary site in vacuum-fractured polycrystalline MgO containing 3000 cation ppm Sc.

Upon quantifying and integrating the Sc segregation profile a value is reached of 7.8×10^{14} e/cm^2, where e is the electron charge for the boundary charge necessary to balance the increased $Sc^{\bullet}_{Mg}$ concentration on this side of the fracture path. Several models were then applied to calculate the space-charge segregation profile of Sc, consistent with the experimental value of the boundary charge. The concentration of unassociated Sc in the bulk was approximated to be one-half the total Sc concentration, in accord with electrical conductivity data for Sc-doped single-crystal MgO. Results are shown in Figure 3.6.3. Curve I is the solution known in colloid chemistry as the Gouy-Chapman approximation. (See, for instance, E. J. W. Verwey and J. Th. G. Overbeek, Theory of the Stability of Lyophobic Colloids. Elsevier Publishing Co., New York, 1948.) This is a solution of Poisson's equation for the space-charge potential profile that is equivalent to the results obtained by Lehovec (J. Chem. Phys., 21 [7], 1123-1128 [1953]) and Kliewer and Koehler (Phys. Rev., 140 [4A], 1226-1240 [1965]) for ionic solids. A serious flaw of the theory is apparent; near-boundary concentrations of Sc are predicted that are much higher than the density of cation sites in the crystal. This results from the treatment of charge as continuous and the assumption that it is able to approach the boundary without limit, instead of considering the charge as made up of finite-size ions. Curve II shows a better approximation with the space-charge region considered as two layers, a Stern layer and a Gouy layer. The Stern layer has a uniform charge concentration, across which the space-charge potential decreases sufficiently for the Gouy-Chapman theory to be more applicable. In Figure 3.6.3 we have taken the Stern layer to be a partial monolayer and have solved the Gouy layer to balance the fraction of the surface charge not compensated by the Stern layer. In addition, we have integrated the Gouy layer over successive atomic distances away from the boundary.

However, since in the experimental data the approach of ions to the boundary is apparently more constrained than is predicted by either continuum theory, a multiple layer adsorption approach was considered as well. The result is depicted by Curve III in Figure 3.6.3. Here the free energy of adsorption of each layer is considered to vary with the electrostatic potential. We have assumed Langmuir-type adsorption and have applied the familiar McLean

Chiang, Henriksen, Kingery and Finello
Figure 3.6.3

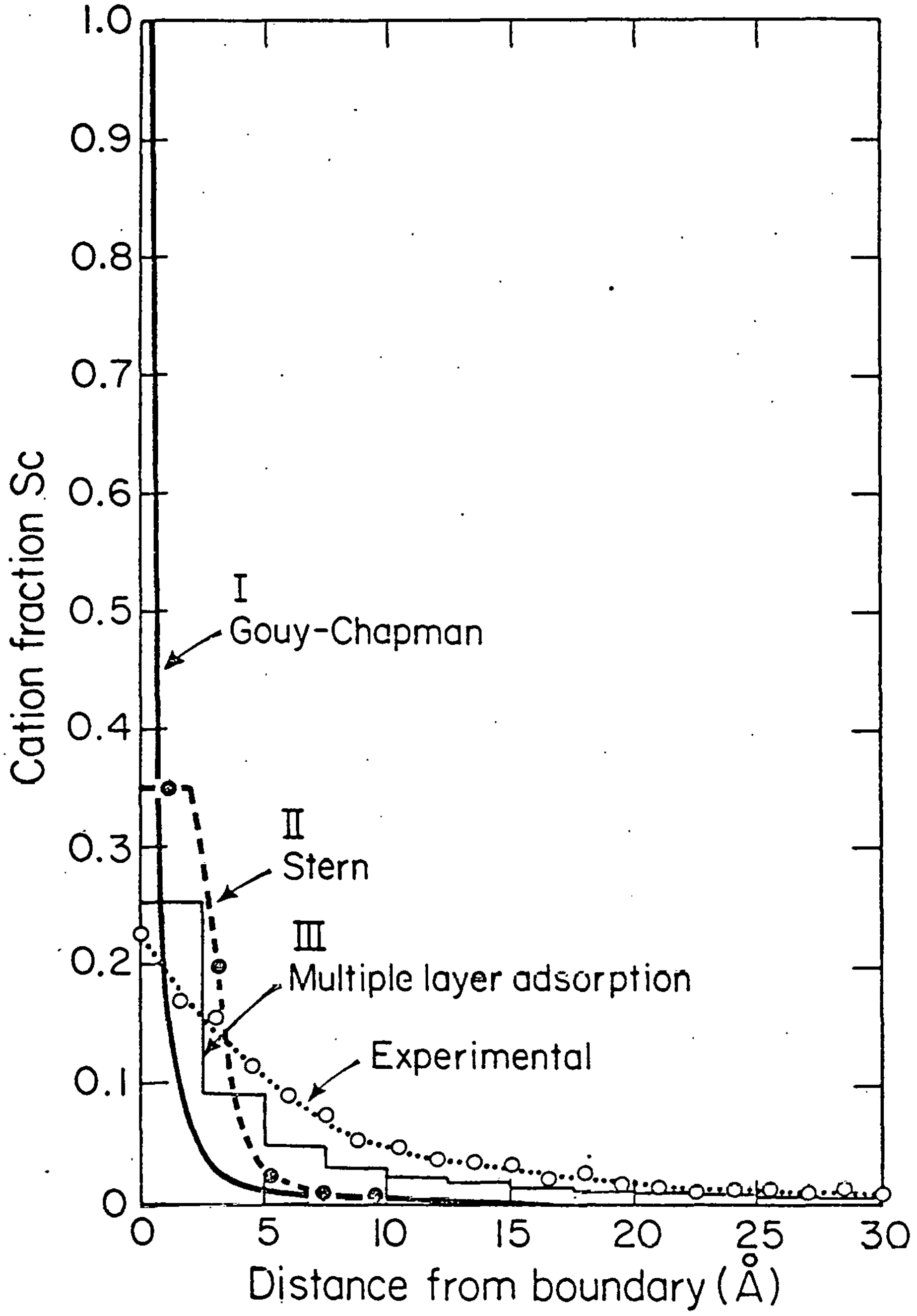

Figure 3.6.3 The experimentally observed Sc segregation profile, the Sc segregation profiles calculated from the Gouy-Chapman and Stern solutions for the space charge potential, and the multiple layer adsorption approximation, as described in the text.

adsorption isotherm (See D. McLean, Grain Boundaries in Metals, Clarendon Press, Oxford, 1957.) in order to determine the Sc concentration of the adsorbed layers.

The multiple layer adsorption approach is apparently the better approximation of the observed segregation behavior, though it still represents a greatly oversimplified picture. Among other things, an improved spatial resolution (currently ∿7 Å for Sc with AES) is necessary for comparison with theory and a more complex analysis. It does seem, however, that the segregation of Sc^{3+} to the boundary in the absence of a significant strain field is consistent with a space-charge theory, and it is clearly a different type of behavior from that of partial monolayer adsorption.

3.7 Grain Boundary Segregation in SiC Investigated by STEM

Personnel: Y. Tajima and W. D. Kingery

Grain boundaries and boundary regions are important in all polycrystalline solids. Aluminum and boron are known to be effective additives in SiC as sintering aids, but the mechanism of their effects is not as yet clear. There have been several conjectures as to the effect of boron: boron segregates on grain boundaries and reduces grain-boundary energy, which decreases the ratio of grain boundary to solid-vapor surface energies (S. Prochazka, pp. 171-82 in Special Ceramics 6, British Ceramic Research Association, 1975); segregation of boron retards surface and/or vapor-phase transport and grain growth at lower temperatures, which results in enhanced densification at higher temperatures (C. Greskovich and J. H. Rosolowski, J. Amer. Ceram. Soc., 59 336-343, 1976); either reaction sintering or liquid-phase sintering is responsible for the densification of SiC + B compound compositions (F. F. Lange and T. K. Gupta, J. Amer. Ceram. Soc., 59 537-538, 1976). The effect of aluminum on sintering of SiC has not been studied as extensively as that of boron, but the tendency of aluminum to retard discontinuous grain growth has been observed (W. Böcker, H. Landfermann and H. Hausner, Powd. Met. Int., 11 [2] 83-85, 1979). In all cases, grain boundaries have the important role. The necessity of studying grain-boundary properties is obvious.

STEM with energy dispersive x-ray spectroscopy (EDX) has been used as an analytical technique to study the grain boundary segregation in SiC. This technique has been limited to the detection of elements of atomic number ≥9, and initial studies have been focused on the characterization of aluminum-containing materials. Samples, supplied from Dr. Hausner, W. Germany, were sintered with the addition of 1.1 wt % Al and 2 wt % C at 2100°C for 20 min. Optical microscope observation showed they had relatively homogeneous microstructure with grain size mostly less than 10 μm (Figure 3.7.1). Samples for STEM examination were prepared as follows. Materials were sliced off the bulk with a thin diamond cutting wheel. These sliced samples of about 100-150 μm thickness were ground with 30 μm and 5 μm diamond pastes to the thickness of about 50-75 μm and then prepared for electron microscopy by ion thinning with argon ions accelerated through a potential of 6-10 kV.

STEM analyses of as-sintered samples showed that there is aluminum segregation at grain boundaries, and no aluminum-containing second phase was observed. After subtracting a computer-generated semi-empirical background from x-ray spectra, integration of x-ray counts in the energy range of 1.44-1.54 keV for Al and 1.60-1.92 keV for Si gave consistent results. Neither segregation nor precipitates of other heavy elements was observed.

To evaluate the effects of heat treatments, samples, 50-75 μm thick, were placed in a W crucible filled with SiC powder and heated in a vacuum at 1350°C and 1500°C for 1 to 5 hours. STEM analyses of those samples showed that amounts of Al segregation were less than that of the as-sintered sample (Figure 3.7.2).

A sample of about 150 μm thickness was heated in the same way at 1500°C for 3 hrs. Substantial "segregation" of Al on a grain boundary was observed, but the Al concentration along the grain boundary was not uniform (Figures 3.7.3, 3.7.4). The same sample, about 150 μm thick and heat-treated at 1500°C for 3 hrs, was then placed in a graphite crucible filled with SiC powder and reheated at 2100°C for another 3 hrs in a carbon tube furnace. After this heat treatment, neither segregation of Al nor precipitates were observed (Figure 3.7.3).

The results imply that Al might have diffused out during heat treatments. Further examination will determine how much Al, if any, diffuses out during heat treatments using AES. The results should suggest if aluminum segregation in SiC follows normal segregation theory (more segregation at lower temperatures).

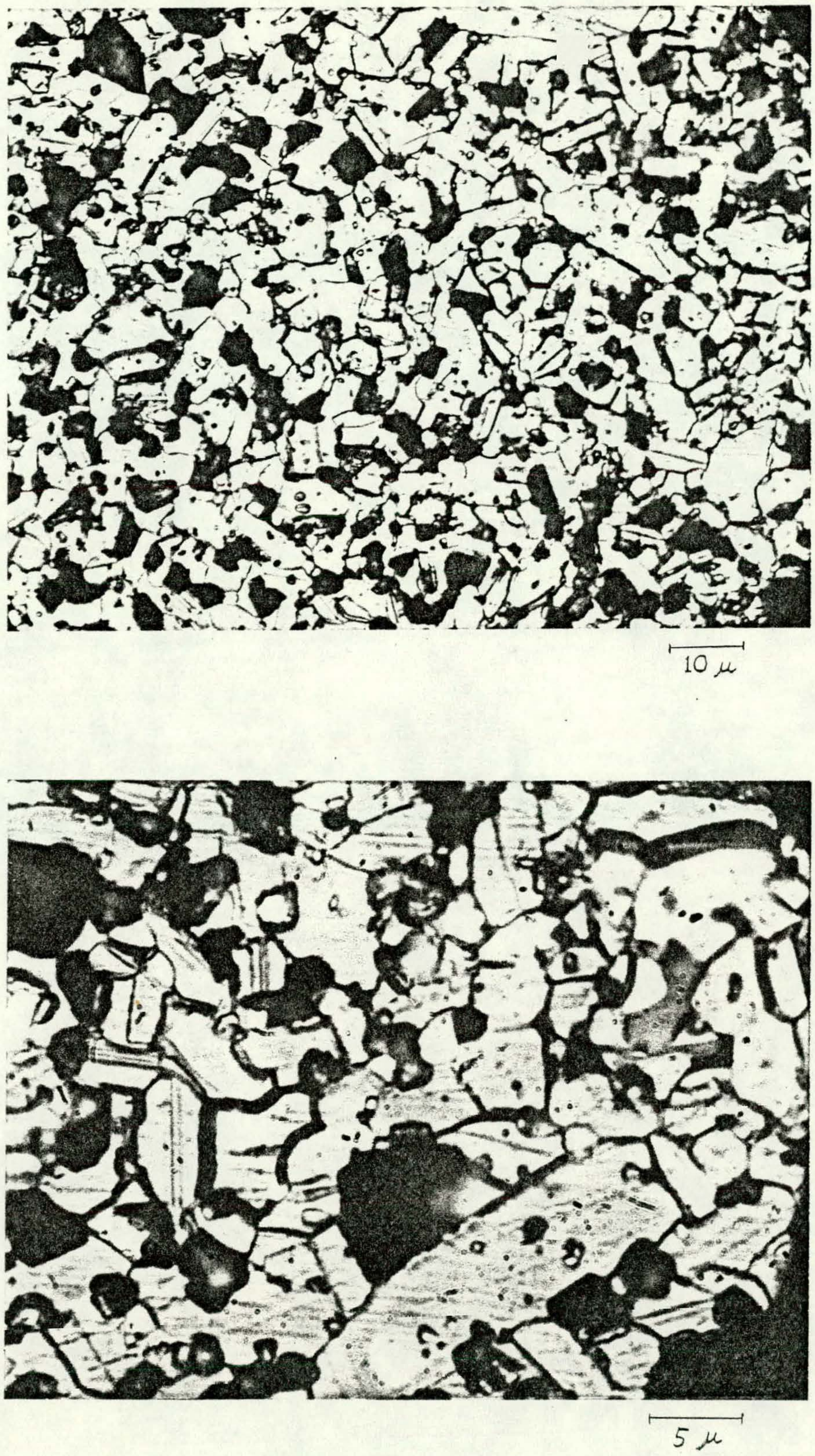

Figure 3.7.1 Microstructure of sintered -SiC
(1.1 wt % Al, Z wt % C)

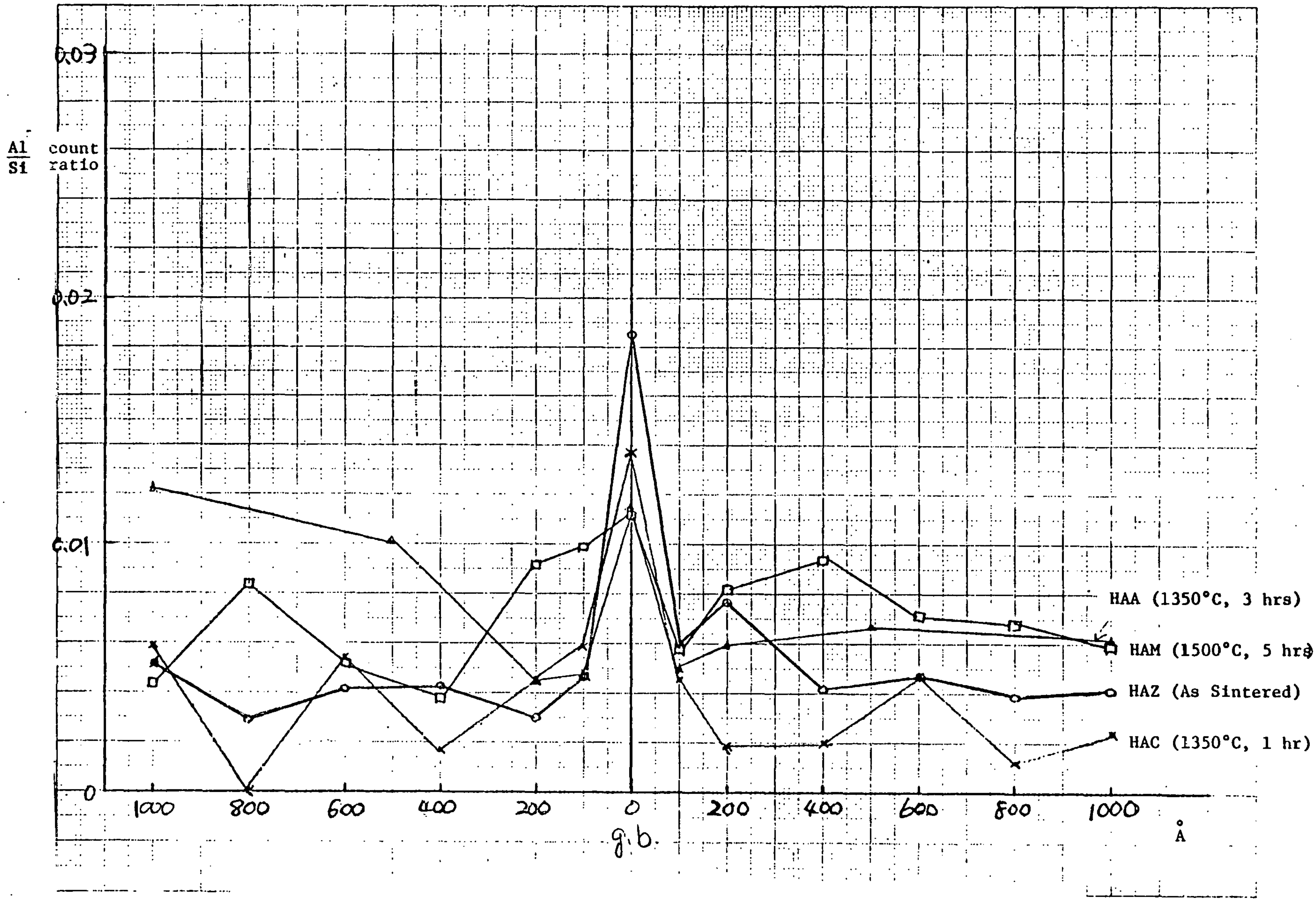

Figure 3.7.2 Al to Si x-ray count ratios of sintered α-SiC with various heat treatments.

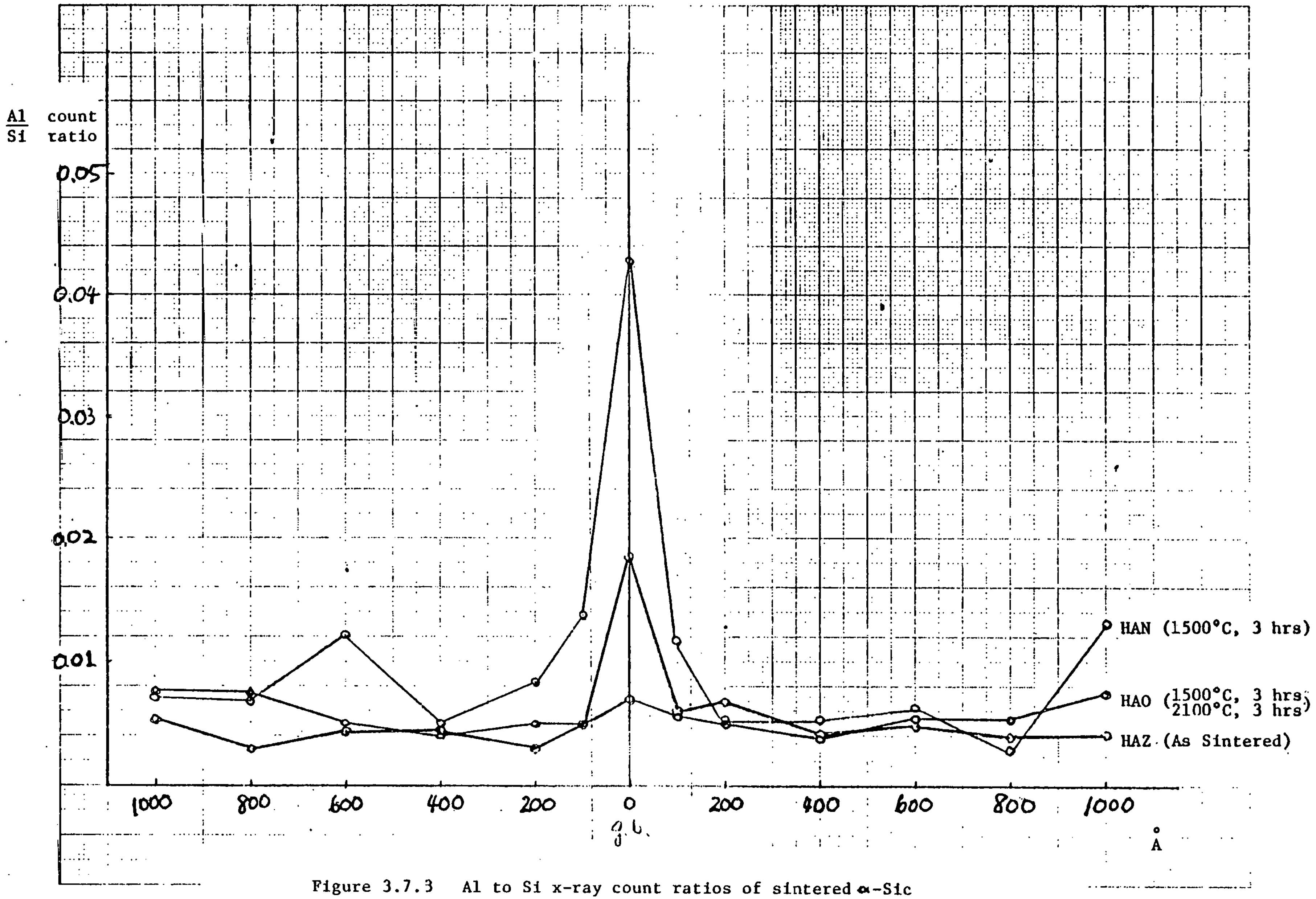

Figure 3.7.3 Al to Si x-ray count ratios of sintered α-SiC with various heat treatments.

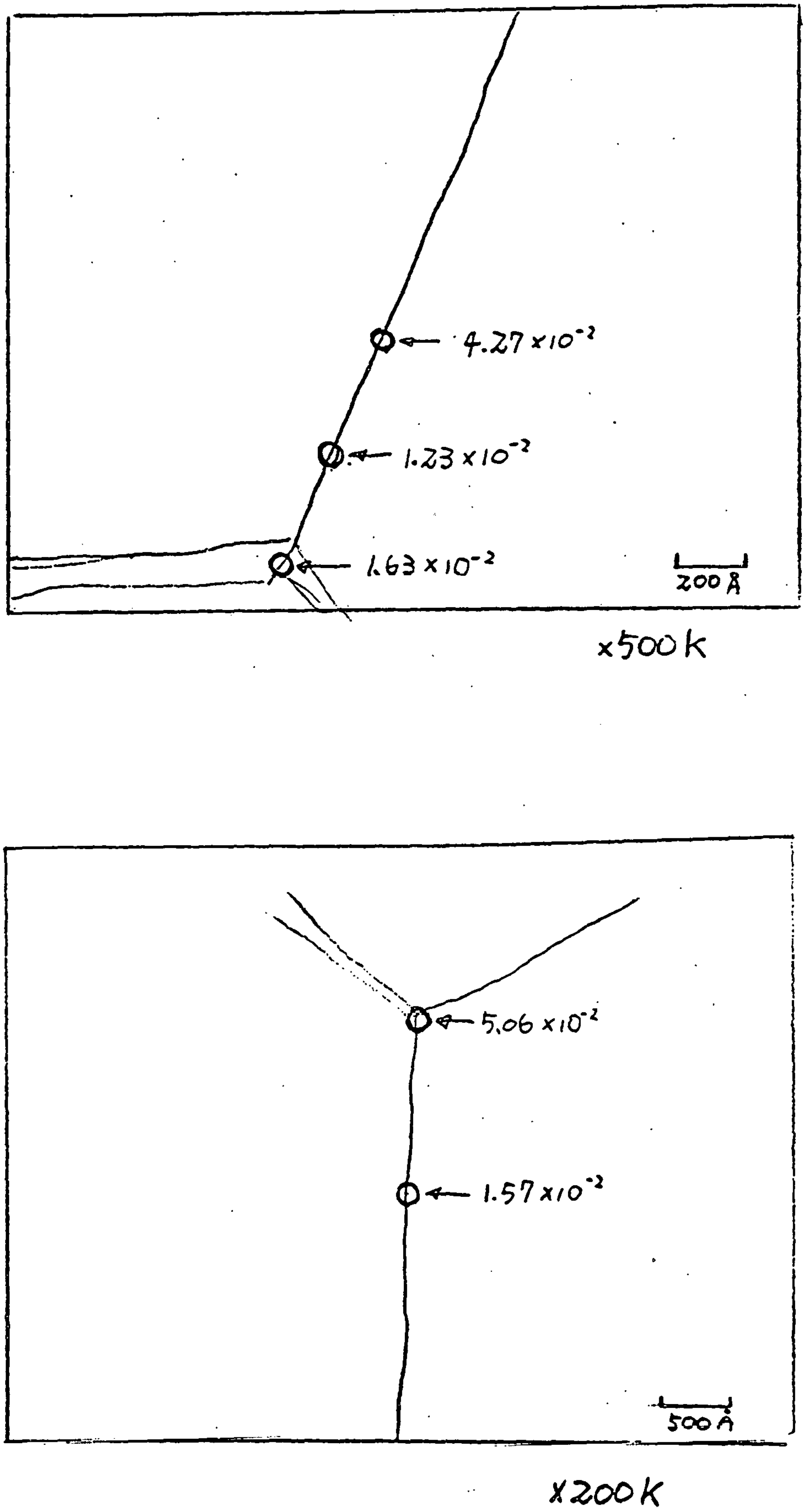

Figure 3.7.4 Al to Si x-ray count ratios at several points on grain boundaries and at triple points.

Use of a windowless detector installed into STEM should detect light elements such as B, N and O, and boron-containing smaples will be analyzed.

3.8 Grain Boundary Composition in Manganese Zinc Ferrites

Personnel: Y.M. Chiang and W. D. Kingery

Manganese zinc ferrites are a class of soft ferrites, characterized by high permeability and low losses, that are widely used as cores for transformers and inductors. It has been found that the properties of the grain boundary, including segregated dopants, often determine, to a large degree, the properties and applicability of the polycrystalline material. We have used x-ray microanalysis in the scanning transmission electron microscope (STEM) to characterize the grain-boundary composition and to clarify the role of boundary composition on magnetic permeability in samples of MnZn ferrite of nominal composition $Mn_{0.490}Zn_{0.431}Fe_{2.079}O_4$, containing residual impurities (500 ppm Ca, 350 ppm Si) as well as additions of CaO (0.02 and 0.04 wt %). (Prepared and heat-treated at Bell Laboratories, Allentown, Penn.) These samples were prepared by a conventional ball-milling process and were sintered in a tunnel-type kiln in a cycle consisting of a 1-hour firing at 1340°C in an atmosphere of 5% O_2, followed by cooling at a rate of 400°C/hr. During cooling the atmosphere was changed to 100° N_2 at 1100°C.

Micrographs of polished and etched cross-sections showed the microstructure of the doped and undoped samples to be very similar, with the average grain size of 6 to 7 μm which is generally considered optimum for a combination of high permeability and low losses. STEM observations on fractured surfaces, however, showed a dramatic change in the mode of fracture upon addition of Ca, ranging from largely transgranular failure in the undoped sample to almost completely intergranular failure in the sample containing 0.04 wt % added CaO.

STEM analyses on ion-thinned samples revealed that the fabrication technique, which is similar to production processes, results in regions of inhomogeneous agglomerates, located primarily at grain junctions that consist of both particles of pure ferrite and particles containing high concentrations of Ca and Si. Occasionally, the presence of Cr and Ni was also detected, the source of which may be the stainless-steel mills used in processing. Differences in the bulk composition of Mn, Zn and Fe in the range 1-2 at. %, as characterized using the Cliff-Lorimer method of thin-film x-ray analysis, were found from grain to grain as well. These inhomogeneities were present in both doped and undoped samples.

In the sample with 0.04 wt % added CaO, occasionally a continuous grain-boundary phase enriched in Ca and Si was seen as well. The absence of rounded corners at the grain junctions where the phase terminates, indicates that it was not present as a liquid film and therefore, may have either been present as a second phase at equilibrium or may have exsolved upon cooling.

In all samples, analysis of "clean" grain boundaries (projected width ≤30 Å in bright field image) showed the segregation of Ca and Si, as seen in Figure 3.8.1, which was, in all cases, confined to within 100 Å of the grain boundary. A clear increase in the amount of segregated Ca with increasing added CaO content was observed, while the amount of segregated Si remained relatively constant. This behavior is consistent with a strain energy model of segregation as the ionic radius of Ca^{2+} (0.99 Å) is large in comparison with that of the host cations. Although the strain energy is also large for accomodation of the small Si^{4+} ion (radius 0.41 Å) in the ferrite lattice, the driving forces for segregation in this case are more complex and may be multiple in nature.

The depletion of Zn and sometimes of Mn, relative to Fe in the near-boundary region, was observed as well, the changes in composition being typically 2-3 at. % and occurring within 200 Å of the boundary. A typical profile across the boundary is shown in Figure 3.8.2 as the x-ray intensity ratios Zn/Fe and Mn/Fe.

In high-permeability soft ferrites, the displacement of domain walls is the dominant magnetization mechanism. Although the exact form of derived expressions depends on the domain wall configuration that is assumed, the permeability (μ) is, in general, inversely proportional to some power of the magnetocrystalline anisotropy constant ($\mu \propto K_1^{-n}$). The magnetocrystalline anisotropy is determined primarily by chemical composition, but in the presence

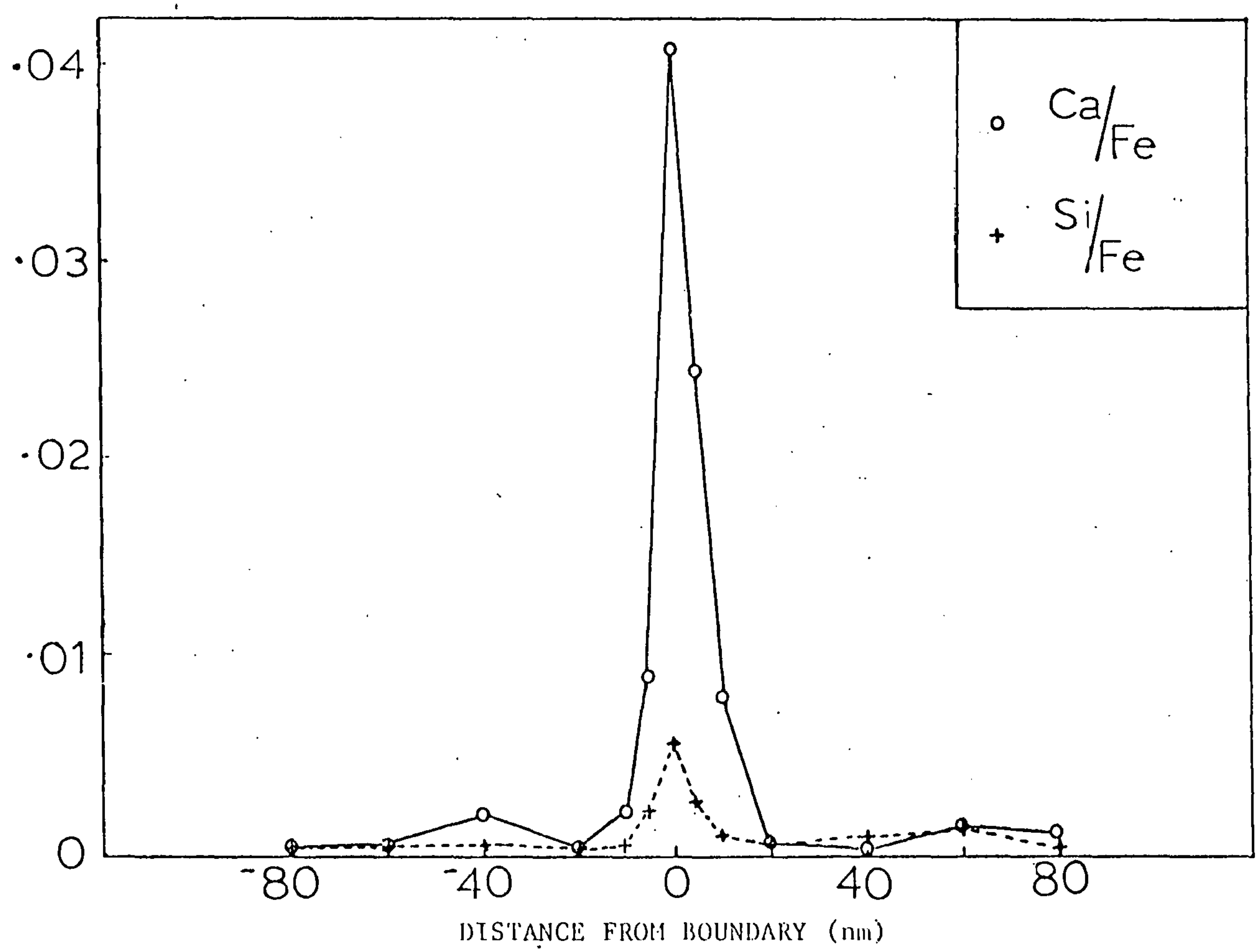

Figure 3.8.1 Typical segregation profile of Ca and Si across a clean boundary.

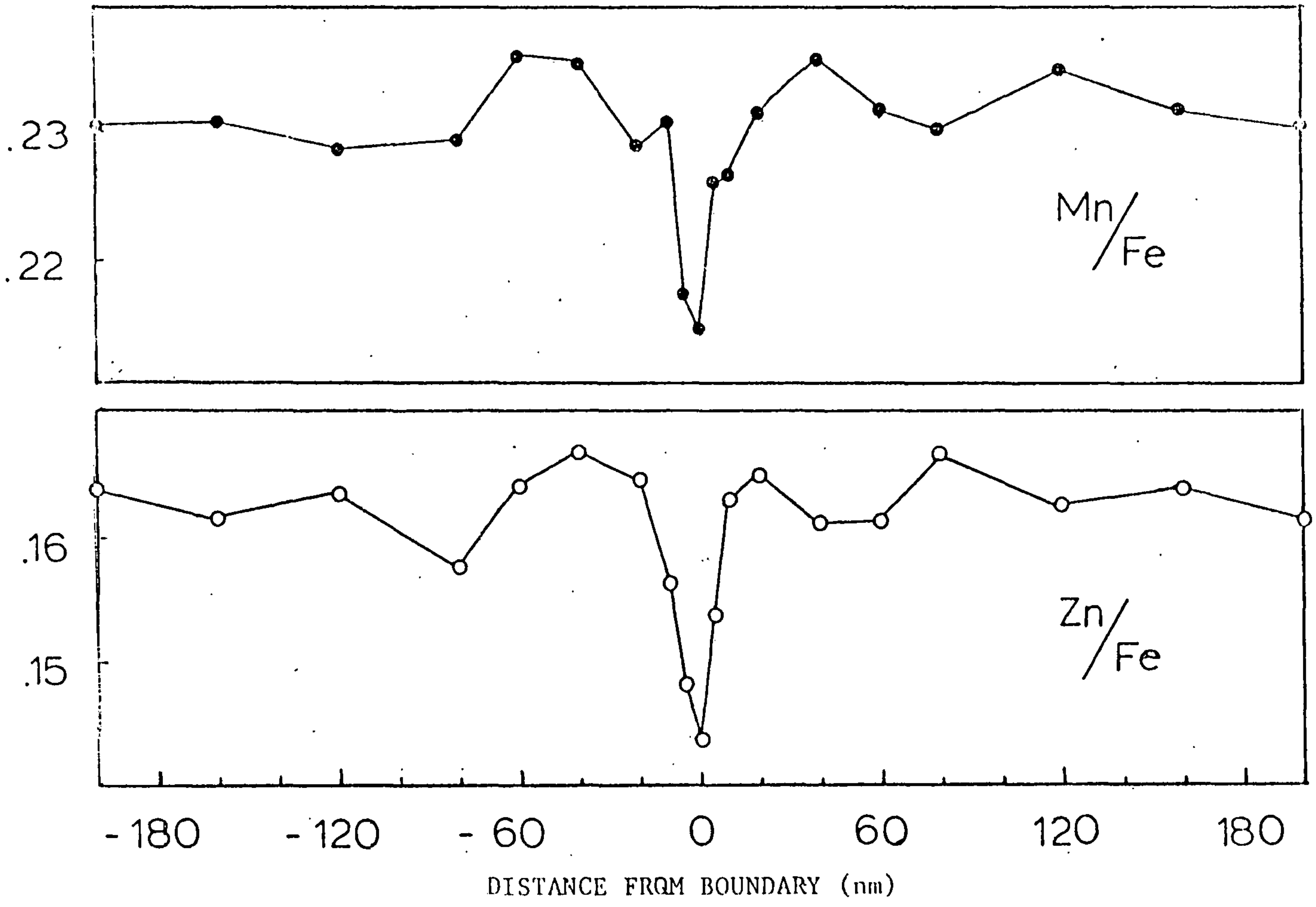

Figure 3.8.2 Mn/Fe and Zn/Fe intensity ratios across the boundary, sample containing 500 ppm Ca.

of external or internal stresses, additional work is performed against the stresses in magnetostrictive deformation and requires that the anisotropy constant be modified by an additive term, resulting in an effective anisotropy which for an isotropic material may be expressed as

$$\kappa_{eff} = \kappa_1 + 3/2\ \lambda_s \sigma \quad ,$$

where λ_s is the saturation magnetostrictive coefficient and σ the stress.

For the present samples, permeability vs. temperature curves have been measured and are shown in Figure 3.8.3a. The fluctuations from sample to sample are consistent with a shift in the effective anisotropy vs. temperature curve, as shown in schematic form in Figure 3.8.3b. Although the experimental results do not indicate a sufficient change in magnetic ion composition from sample to sample to account for this variation, grain-boundary stresses are likely to be present in these samples since available data shows that the depletion of Zn causes a decrease in the lattice parameter while the segregation of Ca causes an increase. The Ca^{2+} ion is much larger, however, (0.99 Å ionic radius vs. 0.74 Å for Zn^{2+}), and most probably has the dominant effect. We conclude that the fluctuations in permeability correspond to a varying effective magnetocrystalline anisotropy, resulting from grain-boundary stresses that increase with increasing segregation of Ca.

The MnZn ferrite system is also a particularly viable candidate for a pilot study of oxygen accumulation and depletion at grain boundaries in metal oxides. A wide range of stoichiometry is possible in soft spinel ferrites, and the concept of preferential diffusion of oxygen along the grain boundaries, and resultant changes in stoichiometry, has often been invoked to explain observed phenomena. It was in 1951 that C. G. Koops (Phys. Rev. 83 [1], 121 [1951]) first observed a dispersion in the dielectric constant and electrical conductivity of NiZn ferrite and, in explanation, postulated the existence of a more oxidized, insulating grain boundary separating the semiconducting grains. Since then, the work of Paulus (Mat. Sci. Res., 3, 31 [1966]) and Akashi (NEC Res. and Dev., 8, 89 [1966] and 19, 66 [1970]) have supported this theory and have demonstrated a strong dependence of this phenomenon on sintering

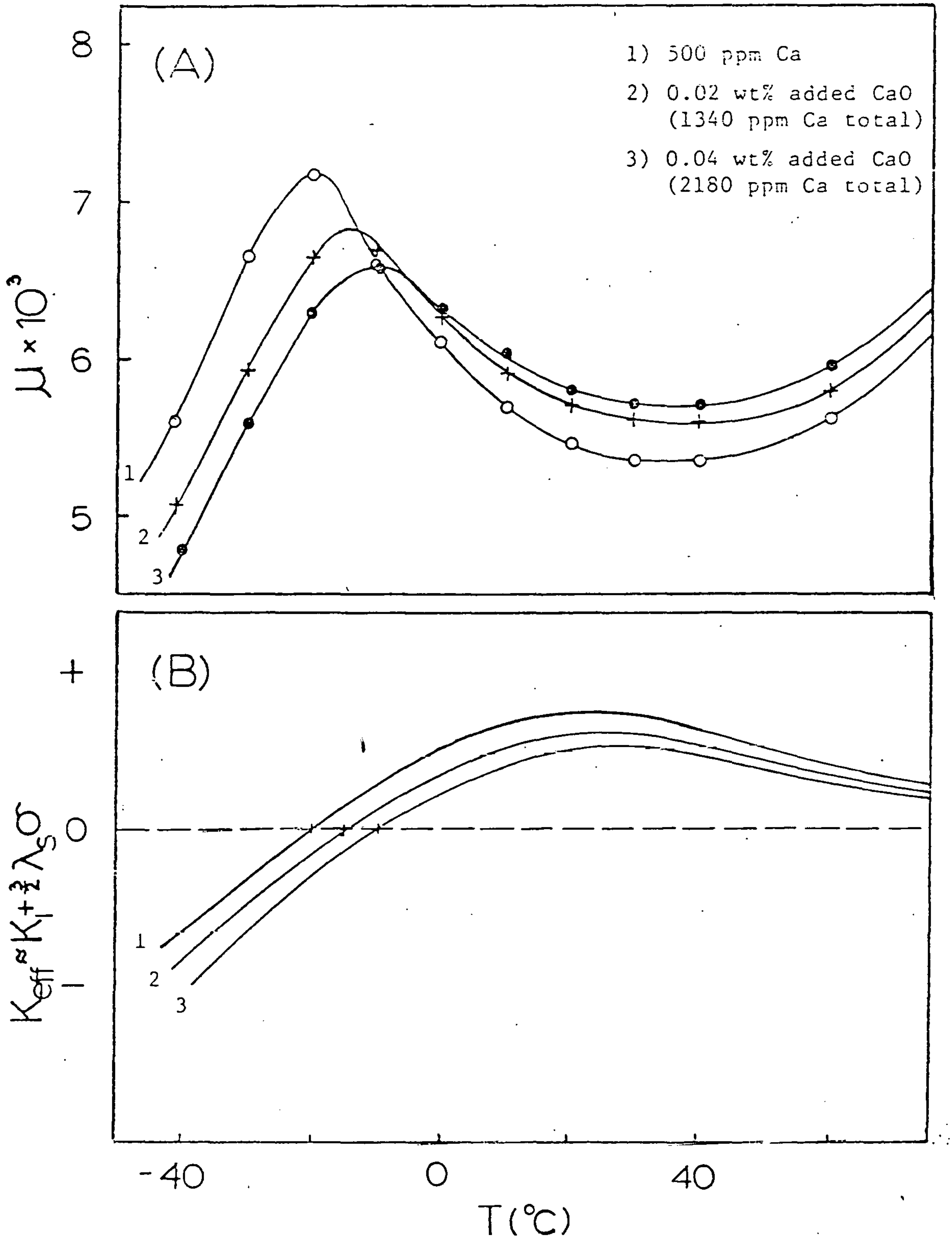

Figure 3.8.3 A) Measured permeability vs temperature curves for the three samples, and
B) Corresponding schematic K_{eff} vs temperature curves.

atmosphere as well, particularly in the presence of segregated Ca and Si. Precipitation of α - Fe_2O_3 at the boundaries of CoNiZn ferrite has been observed, resulting in decreased resistivity, and the preferential grain-boundary diffusion of oxygen has again been cited as a contributing factor (M. P. Harmer, to be published). Often the volatilization of Zn from MnZn ferrite has been observed to have a dependence on partial oxygen pressure. More recently, the mechanical properties of MnZn ferrites have been correlated with changes in the mode of fracture, similar to the behavior observed in the above study, which are sensitive to sintering atmosphere and grain-boundary segregants in a way that is not yet well understood. (See for example, D. W. Johnson et al. Amer. Ceram. Soc. Bull., 59 [3], 363 [1980].)

There has not been to date, however, a direct observation or characterization of the oxygen concentration profile at the grain boundary in metal oxides. This is due in part to the lack of a suitable analytical technique. Although the present x-ray detector in STEM is unable to detect elements of atomic number less than 9 due to window absorption problems, the advent of an ultra-thin window detector will allow detection of lighter elements including oxygen, and such an investigation will indeed then be feasible. A major research objective for the immediate future is to explore the oxygen distribution at grain boundaries in the present samples of MnZn ferrite. A clear characterization of the oxygen profile at boundaries will help to clarify the present conjectures concerning rapid oxygen diffusion along the boundaries in ferrites and will contribute substantially to the understanding of this phenomenon with regard to metal oxides in general.

3.9 Surface Oxidation in Silicon Carbide

Personnel: K. Kijima and W. D. Kingery

We have begun a study of oxygen surface segregation and its effect on silicon atoms in SiC, using Auger Electron Spectroscopy. Initial results indicate that oxygen is adsorbed on the basal surface of silicon carbide, both as grown and as ion-implanted with boron. The oxygen intensity peak was reduced by annealing at high temperature in vacuum.

Electron energy of silicon on the surface of crystals showed chemical shift from that in SiC bulk. It was shown from A.E.S. energy that surface silicon was oxidized to form SiO_2. It can be estimated that the silicon oxide layer might be vaporized by heating.

The oxidized layer thickness on SiC basal surfaces was different between the front and back sides, presumably because of polarity differences.

4.0 Sintering Studies

4.1 On the Question of Breakaway Grain Growth in Magnesia Doped Alumina

Personnel: R.L. Coble

It has been known for a long time that the addition of magnesium oxide to aluminum oxide controls discontinuous grain growth and prevents the breakaway of grain boundaries from pores during the final stages of sintering. Although there have been many kinetics studies of grain growth, the results obtained in different atmospheres by different investigators show somewhat discrepant results; at the present time it is not even widely accepted as to whether or not magnesia inhibits normal grain growth as well as discontinuous grain growth. Part of this difficulty arises from the fact that different preparation techniques have been employed in making the powder mixture and different atmospheres have been used in firing. The defect structures are expected to be different and to effect the sintering kinetics. Using a simplistic view of the lattice defects involved, the different atmospheres are expected to effect the solubility, hence the defect concentrations produced and as a result, the sintering kinetics if lattice diffusion is indeed the mechanism by which densification takes place.

Because of the fact that pore drag of grain boundaries has been found empirically to exhibit a far larger effect on grain boundary mobilities than do the solute effects, the rates of elimination of porosity would then be manifested as different rates of grain growth assuming that growth takes place to the porosity controlled limit. For the variable magnesia effects, it should be noted that the initially inhomogeneous sample could undergo diffusion induced grain boundary migration as it approaches equilibrium, thus providing a dependence upon the initial structure and techniques by which the mixtures are produced.

Until recently, there have been only two dominant theories regarding the potential effects of magnesium oxide in controlling the breakaway grain growth that is exhibited in pure alumina samples. The first view, as introduced by Burke, was that second phase formation (spinel in this case) would inhibit grain growth by a particulate mechanism in just the same way that porosity inhibits boundary migration. The model adopted was that due to Zener for the interaction between a spherical pore or particle and the grain boundaries. The maximum drag force provided by pores on particles is simply equal to $2\pi R_p\gamma_{bg}$ where R is the radius of the pore or particle and γ_{gb} is the grain boundary energy. Although this model has not been quantitatively tested, the grain growth results are qualitatively in agreement; i.e., the higher the porosity the lower the grain growth rate.

An alternate mechanism by which the inhibition of boundary motion has been presumed to occur is by a solute drag mechanism due to Cahn. There are two sets of data which illustrate the fact that the solid solution of magnesia in alumina is sufficient to control discontinuous grain growth. One result is that the grain growth rate as a function of dopant concentration decreases monotonically until the solid solution limit is reached, then remains constant as the volume fraction of spinel increases. For this experiment, it should be noted that because of slightly variable porosity present the definitive effect of the solute additions on growth rate could not be regarded as quantitative. There are other factors to consider as well, to be noted below.

The second result was generated by the incorporation of magnesia by exchange through the vapor under conditions in which only the solid solution limit could be formed. No magnesia was added to the powder, but the sample sintered to theoretical density at the outer surfaces where magnesia pickup was possible Numerous experiments have been conducted to try to measure magnesia segregation at grain boundaries in alumina by fractography and scanning Auger microscopy studies. To date, none of the published results have shown excess magnesia segregated to the grain boundaries although a second-hand report of efforts by a group at Phillips in Einhoven were cited as showing excess magnesia segregated at the boundaries. There are problems associated with fractography; it is not clear that the fracture proceeds exactly along the grain boundaries, hence, segregation might not be observed. There is another fundamental point to be made; Cahn's solute drag theory does not require that the solute be segregated positively. If the solute is rejected from the boundaries, it would also give impurity drag but then obviously not be detectable by Auger microscopy.

Recently, Heuer, then Bannister, concluded that increased pore mobility by increasing the surface diffusion coefficient due to magnesia doping might be the most important mechanism by which the avoidance of breakaway grain growth takes place. In this argument, it is simply presumed that the pores and grain boundaries migrate simultaneously coupled by the drag interaction force by pores on boundaries (Brook's model). The alternative situation would be that the pore mobility is too low to keep up with the boundary motion, hence the boundary would breakaway from the pores.

In reviewing the applicability of the above model to the grain growth situation in magnesia doped alumina, we have found two deficiencies in the model itself. One of the problems with the model is that the average grain size is used to evaluate the boundary curvatures and hence the driving force for boundary motion. It is to be noted that as the four-sided grains shrink to zero size in a polycrystalline array, the curvature goes to infinity and hence the driving force for boundary motion goes to infinity as the grain approaches zero size. Thus, there is an under-estimate of the potential for grain boundary breakaway from pores using the model based on the average grain size. There is also an underestimate of the maximum possible drag force in adopting Zener's model. New modeling is needed for evaluation of the maximum drag force between pores or particles and grain boundaries as a function of the equilibrium dihedral angles. We have shown qualitatively that the effect can be large, i.e., that equilibrium dihedral angles less than 180° will give larger drag forces than does Zener's model.

Utilizing the model as it exists we have assessed the maximum velocities by which the pores could migrate by either lattice diffusion or by surface diffusion. The lattice diffusivity is taken from the creep data for the magnesia saturated case; the surface diffusivity from Dynys's data on grain boundary grooving. Using the average curvature from the average grain size measurements, an assessment of the maximum grain boundary velocity was calculated by assuming that boundary migration is intrinsic based on boundary diffusivities taken from the creep data in the boundary diffusion controlled regime. The comparison shows that the boundaries have orders of magnitude higher potential migration velocities than do the pores for these assessments. Therefore, even if magnesia can't be detected at grain boundaries, it must reduce the grain boundary mobilities significantly in order to avoid pore breakaway.

In the majority of the arguments posed to date, there has been a tendency to emphasize one or another mechanism for breakaway inhibition rather than to consider all of the possible effects as given or implied by the model. Let us consider on an ad hoc basis that magnesia addition could effect all of the following quantities simultaneously: the surface energy; the grain boundary energy; the surface:boundary energy ratio; the surface diffusion coefficients; the lattice diffusion coefficients; and the grain boundary diffusion coefficients. In addition, positive or negative segregation of magnesia at grain boundaries would be expected to give impurity drag. A main point to be made is that some combination of effects may be important rather than any single effect.

Reduction in the surface energy would of course reduce the driving force for shrinkage; it had been hypothesized earlier that the sintering rate or shrinkage rate might be a critical issue, that is, to enable the pores to shrink to zero size within some critical time interval, beyond which breakaway grain growth might have been inevitable. Thus, although there has been little emphasis given to the notion that the sintering rate of itself is important, we imply that a reduced rate would be deleterious.

The importance of the sintering rates can be judged by the models now used to assess spherical pore/particle mobilities; the mobilities depend upon the reciprocal size to the third or fourth power depending upon whether lattice diffusion or surface diffusion is a mechanism by which motion takes place. Therefore, for the smallest sizes, surface diffusion is the probable mechanism of migration. However, this also provides the basis for understanding of importance of the sintering rate; shrinking pores increase their mobilities during migration and therefore might remain attached to a boundary that is simultaneously increasing its curvature and hence velocity.

By reduction of the grain boundary energy we would reduce the driving force for boundary motion. This would appear to be an attractive alternative of itself. However, the surface and grain boundary energies should be considered together because the boundary to surface energy ratio governs the equilibrium dihedral angle at pore to grain boundary intersections. In Zener's model for pore/particle drag, it is assumed that the equilibrium dihedral angle is 180°. There is no evidence to show how the boundary to surface energy ratio changes as a function of magnesia content, but we infer that reducing the surface energy relative to the boundary energy would decrease the dihedral angle and increase the maximum drag force between pores and grain boundaries.

The influence of magnesia doping on the lattice diffusivity has been inferred from the creep data in which faster creep rates are observed in what has been presumed to be the lattice diffusion controlled regime. This would provide, in addition to enhanced densification by lattice diffusion, the prospect for enhanced pore mobility by lattice diffusion. With respect to the boundary diffusivity and the influence of magnesia upon it, enhanced boundary diffusivities would contribute to the potential for enhanced densification; however, the creep results show that for the boundary diffusion controlled regime there is no influence of magnesia on the creep rates and hence presumably no effect on the boundary diffusivities. Neither the grain boundary grooving studies nor surface area reductions during initial stage sintering of alumina show any affect due to magnesia additions from which we infer that there is no effect on the surface diffusivity.

4.2 Grain Boundary Grooving and Surface Diffusion on Aluminum Oxide

Personnel: J.M. Dynys, R.L. Coble and R.M. Cannon, Jr.

Grain boundary grooving studies have continued during the past year primarily on G.E. Lucalox® lamp tubes (a reasonably high purity alumina that is saturated with magnesium oxide). The results of these experiments, reported as a band of surface diffusivity (WD_s), are in reasonable accord with our previously reported WD_s values. At higher temperatures (1450-1500°C), however, only the larger WD_s values agree with those from a previous study on Lucalox® by Robertson and Ekstrom. A possible explanation is that differing impurity levels is responsible. This would imply that WD_s is impurity sensitive or that volume diffusion is more important than previously considered data on sintering and creep behavior has shown. Alternatively, differences in experimental technique could also be responsible, particularly when the role of MgO is concerned. In order to avert possible volatization of MgO, two samples are butted together, wrapped with platinum foil, and buried in a powder composition similar to the Lucalox® samples. Robertson and Ekstrom placed samples in a covered high-purity alumina crucible. Magnesia may preferentially volatilize or other impurities may be condensed onto the sample surface. Auger spectroscopy is being used to characterize surface compositon. To date, no surface excess of MgO or any other impurity has been noted.

A source of uncertainty in this study may be caused by grain boundaries with low energy. These boundaries have a larger groove angle which results in a more gradual surface contour. Smooth contours reduce optical (and SEM) contrast and smaller measured grain boundary groove widths are estimated (and therefore smaller WD_s values). Further characterization of the samples is needed and some modification of the experimental conditions is required. Pretreating samples at the temperature of interest will form an initial grain boundary width that will be used for reference on subsequently measured kinetic data. This also gives inclined boundaries an opportunity to migrate to a position perpendicular to the surface. Fabrication of samples from several material's sources with careful intentional doping is also a critical area that will be pursued.

4.3 Ceramic Fabrication

Personnel: Tsui Kuo-Wen and R.L. Coble

It has long been recognized that the preparation of powder compacts for sintering to achieve high densities without significant grain growth would require the elimination of the inter-agglomerate porosity that is usually present. This should hypothetically involve the use of monodisperse deagglomerated powder coupled with a fabrication procedure that will yield a uniform density compact with a small and narrow pore size distribution. There are numerous commercial raw materials for which the agglomerates will sinter to high density at relatively low temperatures and times, in comparison with the times and temperatures needed for the achievement of full density. We have been studying the deagglomeration behaviors of some conventional ceramic raw materials by ultrasonic dispersion and by ball-milling. Using commercial Alumina raw materials of small particle size (less than one micron) we have studied the influence of the times required for dispersion by ball-milling versus those required by ultrasonic dispersion techniques. We have used the conventional deflocculants (HCl) and found that surprisingly long intervals of ball-milling are required to achieve complete dispersion (3 days). In relatively short times ultrasonic dispersion has been found to give relatively good dispersion of the powder but to date we have been plagued by problems associated with contamination from the ultrasonic drive horn. We have purchased a sapphire tipped horn to deal with the dispersion of alumina powders.

From the dispersed powders, we have studied conventional slip casting and also consolidation by agitation of the thixotropic gel which forms upon initial water extraction. The densities of the as-fabricated slip cast compacts have been increased to approximately 65% theoretical density. By agitation of the thixotropic gel the average bulk density has been increased to approximately 73%, although at this stage the bulk densities in those compacts are non-uniform. The more dense packed regions of these compacts are found to sinter to high density at relatively low temperatures and times as expected.

4.4 Model Experiments on Sintering with Gold

Personnel: W. Hong and R.L. Coble

A major problem in sintering technology has been the gap between material geometries assumed in many sintering models, and those usually realized in industrial practice. That is, the goal of producing monodispersed spherical particles of sufficiently small size to enhance driving forces for sintering has not been widely attached, especially in ceramic systems.

A number of investigators have conducted sintering studies by methods that recreate model geometries through the use of wire compacts, spheres or wires on flat plates, etc. For the most part, these experiments were performed on idealized materials specially made for the studies, and not on powders typically used in the manufacture of a specific product.

The majority of the materials used in these experiments have been metals. Among the available metals, gold has the advantages of low sintering temperatures, a simple fcc lattice, extremely noble behavior; and the diffusion behavior has been extensively studied in previous years. The "effective" bulk diffusion activation energy of gold has been well characterized to be in the neighborhood of 42 kcal/mole, mostly through radiographic (tracer) methods. Surface diffusion data shows less certainty, especially for different temperature ranges. Activation energies for D_s in low temperature regimes ($<500^{o}C$) have been measured in the range 15-20 kcal/mole, whereas at higher temperatures ($>900^{o}C$) activation energies of 65-70 kcal/mole are found. The low temperature results were measured through radiography and sintering; the high temperature data were obtained using scratch-smoothing or grain-boundary-grooving techniques. The latter experiments showed rapid drops in D_s below $900^{o}C$ ($\pm 30^{o}C$) to values which could not be measured by those techniques. The sharp declines in diffusivities have been attributed to the effects of impurities because contaminants may segregate to the surface in greater concentrations than in the bulk.

Dupont has supplied samples of a gold powder which they have developed for use in thick film circuitry, consisting of virtually monodispersed, 1μm spheres. This material, at least from the standpoint of geometry, appears to be a candidate for studying sintering kinetics and diffusion in gold through direct observation of neck growth rates via the scanning electron microscope (SEM).

A one inch Kanthal wound tube furnace is being used for these sintering studies, connected in series to a set point temperature controller and variac, which allows temperature control of ± 1°C in air. As received, powder agglomerates have been fired on platinum foil substrates at temperatures low enough to prevent agglomerate adhesion to the platinum. The observations made so far have shown the following:

(1) Substantial initial stage sintering, characterized by easily seen neck growth between spheres, takes place at temperatures in the range 250-300°C, at times of one hour or less.

(2) The effect is mainly of coarsening; i.e., virtually no center-to-center approach of spheres has yet been observed at these low temperatures.

(3) A percentage of the spheres show evidence of undercutting near the neck surfaces.

Assuming that vapor transport can be neglected, and that the spheres have not gone far beyond the initial stage of sintering, it appears that surface diffusion is the dominant mechanism for neck growth. This is in agreement with results on gold by a number of other investigators.

Quantitative measurements at present are less certain. For surface diffusion, the Nichols and Mullins neck growth equation has been used to convert the sintering data to surface diffusivity:

$$\left(\frac{x}{a}\right)^6 = \left[\frac{25\delta D_s \Omega \gamma}{RTa^4}\right] t \qquad \frac{x}{a} < 0.3$$

These calculations give values that are several orders of magnitude lower than that predicted from Li and Parker's tracer diffusion measurements. It is not clear why a discrepancy exists between these preliminary calculations and those of the other investigators in the low temperature range, although large differences might be expected between these low temperature data and those for the much higher temperatures cited above. Impurities undoubtedly play a part; yet Nordstrom and Yost have found that their work on the sintering of a similar (though less monodispersed, spherical, and chemically pure) gold powder yielded D_s activation energies of ~15 kcal/mole, obtained through resistivity measurements on the printed film.

4.5 Experiments on Diffusion Induced Grain Boundary Motion (DIGM)

Personnel: C.A. Handwerker, R. French, R.L. Coble

The identification of DIGM on binary metal systems has stimulated a search for this phenomenon in non-metals particularly in ceramics. In binary oxides, $MgO-Al_2O_3$ is one of the best characterized systems in terms of grain boundary and lattice diffusion, creep, and grain growth data. Within this system, MgO was chosen as the solvent phase primarily because MgO bicrystals are readily available and Al_2O_3-saturated $MgAl_2O_4$ was chosen as the solute phase. The solubility of Al_2O_3 in MgO is approximately 1% Al_2O_3 at 1700°C and 0.1% Al_2O_3 at 1150°C. The order of magnitude in solubility is used to identify the conditions when movement of the grain boundary leaves behind an alloyed region with a concentration below the solubility limit at the higher temperature but higher than the solubility limit at the lower temperature. By following the diffusion anneal by a lower temperature precipitation anneal, $MgAl_2O_4$ precipitates form. By chemical etching, the location of the spinel precipitates and the grain boundary can be clearly seen.

The experiments were performed with an MgO bicrystal of approximately 300 ppm cation impurity from Norton Company, Worcester. The exact orientation of the low angle boundary has not been determined. The MgO bicrystal was packed in pre-equilibrated Al_2O_3-saturated $MgAl_2O_4$ powder in a platinum crucible and was annealed in air at 1700°C for 9 hours. The diffusion anneal was followed by a precipitation anneal at 1150°C for 24 hours. Several specimens were prepared by cleaving the bicrystal perpendicular to the boundary. The newly cleaved surfaces contain the outer surface near the spinel source and the grain boundary along which the solute diffused. The samples were etched in concentrated sulfuric acid which attacks the parent MgO but not the $MgAl_2O_4$ precipitates. The X-ray analysis and high-resolution SEM were performed on two different scanning electron microscopes with X-ray analyzers (JEOL and Cambridge). The JEOL scope has a stated resolution of 60 Å while the Cambridge SEM has a resolution of approximately 200 Å.

The X-ray analysis of the samples show $MgAl_2O_4$ precipitates along the grain boundary with no detectable grain boundary movement. The Al profile across the boundary is symmetrical. The depth of penetration of Al along the boundary at concentrations above the solubility limit at 1150°C was 320μm. In the bulk the depth of penetration is 200μm. While bulk diffusion of Al in MgO at 1700°C is higher than lattice self-diffusion of Mg, the bulk diffusion coefficient measured by interdiffusion experiments predicts a lattice penetration of 20μm after 9 hours at 1700°C. The observed bulk penetration is an order of magnitude higher than estimated from the measured diffusivities. Since no previous study of grain boundary diffusion of Al in MgO has been performed, grain boundary diffusivity of Mg was used to estimate the penetration along the grain boundary. The observed penetration is several orders of magnitude greater than that value. The ratio of δD_b to D_L can be crudely approximated by $x \sim \sqrt{Dt}$. For grain boundary penetration of 320μm and bulk penetration of 200μm, $\delta D_b/D_L$ is 2.6. In all previous cases where DIGM was observed, $\delta D_b >> D_L$. Because this criterion is not met at 1700°C, this phenomenon is not expected to be observed under these conditions.

Commercially available bicrystals of MgO have approximately 300 ppm cation impurities. A lower temperature diffusion anneal of MgO presents more problems. At temperatures below 1300°C precipitation in the parent MgO bicrystals has been observed. Even at slightly higher purity levels, the presence of as little as 1 ppm of some impurities, such as Zr, can cause precipitation near boundaries at these lower temperatures. Wuensch observed that the boundary precipitates in MgO can greatly enhance grain boundary diffusion. At higher temperatures ($T>1300^{\circ}C$) where the solubility of these impurities is higher, there is no enhanced boundary transport. The discrepancy between the estimated and the observed penetration in this study can perhaps be explained by the formation of a continuous boundary precipitate, the spinel, which acts as a fast diffusion path during the high or low temperature anneals. Because the pre-equilibrated source powder had an excess of Al_2O_3, the formation of a spinel precipitate during the "diffusion" anneal becomes possible.

In addition to the effect of precipitates on the diffusion path, precipitates at the higher temperature would also strongly influence grain boundary motion. If boundary precipitates do form, the grain boundary is pinned, grain boundary motion will be impeded and, hence, no DIGM can occur.

An alternate explanation for the absence of DIGM is that the third species, oxygen, rather than Al and Mg controls grain boundary diffusion and grain boundary motion. In this case, no grain boundary "Kirkendall" effect would be seen since this effect requires an unequal diffusion of two species. The two measurements of oxygen grain boundary diffusion in the literature give both higher and lower values at 1700°C than Mg grain boundary diffusion.

4.6 Sintering of Covalent Materials

Personnel: W.S. Coblenz, R.L. Coble, and R.M. Cannon, Jr.

Covalently bonded materials, notably SiC and Si_3N_4, are candidate materials for various high-temperature structural applications, having good oxidation resistance, creep resistance, high strength, and thermal shock resistant properties at high temperatures. These materials have been hot-pressed to high density, usually with a liquid phase present. Most parts have been machined to shape after heat treatment. Reaction sintered silicon carbide has been commercially available for many years. This material is formed by siliconizing mixtures of carbon and silicon carbide grain. Strength, high-temperature creep and oxidation resistance of the reaction sintered materials are generally inferior to the hot-pressed material. The development of sintered silicon carbide is notable because it combines the best properties of hot-pressed SiC and the flexibility of using fabrication techniques (i.e., die pressing, ejection, molding, slip casting) to produce near-net shaped products, which is a decided advantage for reaction sintered material.

It is the objective of this study to investigate the sintering mechanisms important in covalent materials. Silicon has been chosen as a model material for several reasons. Impurity solubilities and their acceptor or donor levels are known for many dopant elements. Diffusion data are available for impurities, self-diffusion mechanisms have been studied to some extent, and silicon is available in high purity.

The two general characteristics of semiconductors which have the greatest consequence for their sintering behavior are intrinsically low self-diffusion coefficients compared to metals and oxides at the same fraction of their melting points, and the tendency of their surfaces to combine with impurities to form a large variety of surface phases. The low self-diffusivities require small particle sizes for reasonable shrinkage rates, but may also promote undesirable and competing coarsening processes. For example, comparing copper and silicon at their melting points, their self-diffusivities and vapor pressures are:

$$D^*_{cu} = 2.1 \times 10^{-8}\ \text{cm}^2/\text{sec} \qquad P^o_{Cu} = 4.34 \times 10^{-7}\ \text{atm}$$

$$D^*_{Si} = 5.17 \times 10^{-12}\ \text{cm}^2/\text{sec} \qquad P^o_{Si} = 4.9 \times 10^{-7}\ \text{atm.}$$

It has been shown (Greskovich et al., J. Am. Ceram. Soc. 59, 7-8 (1976)) that silicon powders exhibit the coarsening versus shrinkage competition typically found for covalently bonded materials, and that boron is an effective sintering additive. The sintering behavior and the results of Auger and LEED studies (J.J. Bellina, Jr., Jap., J. Appl. Physics, 13 (1974)) both strongly suggest that the role of boron is to segregate to surfaces at the sintering temperature, impede vapor and/or surface transport, and thus reduce the coarsening, allowing the shrinkage mechanisms to dominate.

Silicon may coarsen by either vapor phase transport or surface diffusion depending on chemistry and particle size. Grain boundary grooving profiles for pure silicon obtained by both ourselves and by Robertson (submitted to J. A. Ceram. Soc.) have shown that surface diffusion dominates vapor phase transport. Greskovich et al., however, concluded on the basis of scaling law experiments (shrinkage versus initial particle size) that vapor phase transport controlled the coarsening process. Extrinsic vapor phase transport (silicon transported as SiO) may have been involved. Oxide surface films as well as dissolved oxygen could give rise to active oxidation conditions. Also silicon reacts with alumina as follows:

$$2\ Si + Al_2O_3 \longrightarrow 2\ SiO_{(9)} + Al_2O_{(9)}.$$

Silicon heat treated in an alumina crucible, in vacuum, shows faceting as a result of this reaction.

Boron may reduce surface transport of silicon by either reducing the self diffusion coefficient of Si or by becoming the rate controlling species over the coarsening path. Strong surface segregation observed for boron on silicon supports both of these hypotheses.

We have qualitatively interpreted the surface structure seen on boron-doped samples to be due to an instability analogous to constitutional supercooling at liquid-solid interfaces. The implication for sintering behavior is that both composition and curvature must be considered in determining the driving force for mass transport.

If the solvent (silicon) is Rautian and the solute (boron) is Henrian, then the vapor pressure of silicon, P_{Si}, is:

$$P_{Si} = P^{o}_{Si} (1-x_b) \; (1 + \frac{\gamma\Omega}{RT} k)$$

where P^{o}_{Si} is the vapor pressure of pure silicon, x_b is boron concentration, and k is surface curvature. The implication for sintering is that each component must be transported in its stoichiometric ratio.

If the above model is accepted, then the effectiveness of boron as a sintering additive for silicon is due to the (low) lattice diffusivity of B in Si which then controls the surface transport of silicon. This is an interesting conclusion since coarsening mechanisms are thought to dominate because of intrinsicly low lattice and/or grain boundary diffusivities.

Diffusional induced stresses associated with boron doping of silicon single crystals may generate dislocations. Prusin (J.A.P. 32, 1961) showed that diffusional stresses were analogous to thermal stresses, the maximum stress occurs at the surface and is given by:

$$\sigma_{max} = (\frac{\Delta a}{a_o}) \frac{E}{1-\nu}$$

where E = Youngs modulus

ν = Poisons ratio

$(\frac{\Delta a}{a_o})$ = fractional change of lattice parameter.

Lattice parameter changes of SiC with the addition of boron indicate diffusional stresses of up to 100 kpsi may be possible. Diffusional induced dislocations could enhance densification by either pipe diffusion or combinations of glide and climb giving rise to plastic flow. The surface concentration dependent diffusivities for boron and beryllium in SiC, reported by Vodokov and Mokhov (in "SiC-1973"), were most likely due to dislocation generation. The large stacking fault density observed in sintered SiC may be due to partcial dislocations growing out to take advantage of the low stacking fault energy.

An important implication of such a model is that sintering poisons are those elements which can codiffuse with boron and compensate for its lattice strain. Diffusion induced dislocations provide the mechanism by which the chemical driving force is used to aid densification kinetics.

The diffusional induced dislocation model provides a mechanism whereby a chemical driving force may be used to enhance sintering kinetics. Chemically driving grain boundary migration is a similar process in that a chemical driving force promotes grain growth. It is interesting to note that some systems in which DIGM (diffusional induced grain boundary migration) has been observed also show activated sintering. Ni activated sintering of tungsten being a prime example.

We have come to the following conclusions regarding the sintering of silicon:

(1) Coarsening occurs by surface diffusion in pure silicon for all particle sizes of interest.

(2) Chemical vapor transport as SiO can dominate neck growth and lead to large weight losses under some conditions.

(3) Boron segregates to silicon surfaces. It's role in sintering is to reduce surface diffusion. It may do this by either reducing the intrinsic surface diffusivity and/or becoming the rate controlling species over the coarsening path.

(4) Diffusion induced dislocations may provide a means (and an opportunity) to enhance densification processes.

X-ray lattice parameter measurements should be made in systems showing activated sintering. TEM studies on diffusion couples should be undertaken to confirm dislocation generation. Both boron and beryllium should be used as dopants in SiC. The effect of co-dopants which add to or compensate lattice strain should be investigated.

If the diffusional induced dislocation model is correct, silicon powders pre-doped with boron should be "less active" than powders of the same size which are sintered while doping. Powder preparation should minimize oxygen content to avoid chemical vapor transport as a complication. Pure and pre-doped powders shall be prepared via the vapor phase with silane and BCl_3 as starting materials.

Concepts derived while working with silicon whould be applied to Si_3N_4. The effects of dopants, and the manner in which dopants are added on the coarsening process will be followed by surface area measurements and SEM microstructure characterization of powder compacts. Lattice parameter measurements should give an indication of a dopant or combination of dopants ability to induce lattice strains and thereby activate sintering.

5.0 Mechanical Properties

5.1 The Influence of Grain Size Distributions and Grain Arrangements on Grain Boundary Diffusion Creep

Personnel: J.H. Schneibel, R.L. Coble, R.M. Cannon, Jr.

In the equations for diffusional creep of polycrystals there are specific numerical factors that appear that depend on the grain shape assumed. Burton has assumed that the models are in error because creep takes place faster than that predicted by the models using independently measured diffusivities. The numerical factor depends on the geometry of the grain boundaries (GBs) in the polycrystal considered and on the definition of the grain size (for example metallographic mean free path or (average grain volume)$^{1/3}$). The accurate calculation of A for real crystals is desirable in order to be able to determine correct diffusion coefficients from creep experiments and in order to predict creep rates by means of previously measured diffusion coefficients. The latter approach could be employed to verify the interface control of diffusion creep at low stresses.

In the past much work has been done to determine for one grain or for arrays of identical grains the value of A as a function of the grain shape. For example, A has been calculated for spheres, squares, and hexagons. The different grain shapes cause the geometry factor to vary by a factor of 5. In a real polycrystalline, however, sample grains with different sizes are found as well as different shapes. Since these grains have to deform in a compatible way (as long as voids are not formed) it is far from obvious what the relevant value of A should be if an experimentally determined average grain size like the metallographic mean free path is employed in the creep equation.

In former derivations of the diffusion creep equation only the influence of the shape of the grains was considered and the size distribution and grain arrangement were kept constant (i.e., identical grains). In the present work, the size distributions and different arrangements of grains with identical shapes were considered in calculating the corresponding values of A. In order to facilitate the analytical calculations only 2-dimensional grain geometries were considered. The only grain shape found to be suitable was that of squares with integer size ratios.

The strain rate was calculated as a function of the applied shear stress for different grain configurations using an extension of the method described by Spingarn and Nix (1978). Elastically rigid grains (with freely sliding GBs) are assumed and therefore the rate of insertion or removal of matter along a particular GB segment is constant. This in turn requires that the vacancy concentration along a particular boundary segment be parabolic. The problem then amounts to selecting a suitable repeat unit in the array considered and to fit the parabolic vacancy concentrations corresponding to each GB segment such that:

(a) the individual grains of the unit deform in a compatible way,
(b) matter is conserved in the repeat unit,
(c) the fluxes at GB nodes do not cause a net removal or insertion of matter at the node,
(d) the flux in the middle of a symmetrically located GB segment is 0, and
(e) the vacancy concentrations at GB nodes are continuous.

GBs which coincide with an edge of the repeat unit and are symmetrically cut by it may be assumed to have a GB width of $\delta/2$. Then the fluxes from adjoining GBs in adjacent repeat units need not be considered. The number of equations necessary to find the diffusion creep equation for a particular grain configuration is 3 times the number of grain segments considered and can often be greatly reduced by symmetry considerations.

The model calculations were performed with regular arrays of square shaped grains having two different sizes. The grain boundary diffusion creep equations for the arrays considered were determined in terms of the metallographic grain size. The geometrical constant, A, in the diffusion creep equation was seen to depend on the particular size distribution and arrangement and variations between approximately 4 and 33 were found. The calculated examples indicate that the variation of A for different grain size distributions and grain arrangements may in special cases be stronger than the variation caused by differing grain shapes.

In order to extend the calculations discussed above to grain shapes more realistic than squares, use would have to be made of a computer. Realistic grain arrays require the consideration of many more grain edges than has been necessary in the highly symmetric arrays discussed above. Since each grain edge corresponds to 3 unknowns in the vacancy concentration, a realistic cluster consisting of, for example, 20 to 30 grains (in 2 dimensions) could be evaluated to obtain a value of A. The material from which the geometry of the cluster has been determined metallographically could be tested in creep to determine A and the calculated and experimental values of A could be compared. The above results indicate that materials with different grain size distributions and grain arrangements might require quite different proportionality factors in the corresponding diffusion creep equations.

5.2 Creep in Tungsten

Personnel: B. Zelinski, R.L. Coble and R.M. Cannon, Jr.

Small additions of nickel or palladium significantly enhance the sintering rates of tungsten and molybdenum, thus making it possible to obtain very dense materials at low temperatures. These rapid rates are due to the increased solid state transport of material, but little can be conclusively said at present about the rate-controlling mechanism(s). While a considerable amount of work is being done on the nickel-tungsten system at temperatures above its eutectic (1512°C), little is being done to discern the operative mechanism(s) at lower temperatures. We have designed and built an apparatus to investigate this problem. The apparatus measures low creep rates (10^{-9}/sec), and through subsequent analysis of the creep data the kinetics of transport can be determined. In general, better theoretical models combined with simpler geometrics make interpretation of creep measurements more productive than performing sintering studies as a source of transport coefficients.

Preliminary creep tests were conducted on tungsten wires to establish equipment reliability and to obtain a data base on tungsten wires with a grain size of about 1 micron at 16,700 psi and temperatures ranging from 1000° to 1400°C. These tests suggested that grain boundary diffusion controlled creep is the operative mechanism at low stresses and temperatures. A subsequent study on the same material at 14,700 psi and temperatures from 100° to 1300°C confirm this conclusion. Unfortunately, oxidation of the tungsten wire was found to take place, thus causing a decrease in the wire diameter as the oxide sublimated. This diameter reduction resulted in a steady decrease in wire temperature as well as a gradual increase in the sample stress. To circumvent this problem the entire vacuum system has been rebuilt and several different combinations of reducing gases and flow rates are being tested. At present, a constant DC power supply is being used which compensates for the wire diameter reduction and thus maintains a constant sample temperature.

After the proper atmosphere control is established, nickel-doped tungsten wires will be studied at various stresses and temperatures. The nickel dopant will be applied to the outside of the wire by electroplating in a Watts' bath. Subsequent heat treatment at relatively low temperatures (<900°C) will initiate the required nickel diffusion into the tungsten grain boundaries.

Further tests on pure tungsten at 4320 psi and 1200°C produced some rather unexpected results. At this stress the wire length gradually decreased with time. Wire shrinkage is expected to occur at low stresses when the work required to extend the surface on grain boundary areas is larger than the work done in moving the applied load. But a zero creep calculation for tungsten wire predicts a maximum stress for shrinkage of about 840 psi. The observed shrinkage at 4320 psi could possibly be due to the presence of dislocations, introduced during the drawing process, whose line tensions would contribute to the overall force balance in favor of shrinkage at higher stresses. Further tests at different stresses are being conducted, as well as microstructural studies, in order to confirm and explain these observations.

Recent documentation suggests that nickel diffusion may induce grain boundary migration in the W-Ni system. At present it is unclear as to what role this migration plays in the reactive sintering of tungsten. In order to investigate this phenomenon experiments on tungsten foils are being conducted. Recrystallization studies have been carried out in order to establish an appropriate stable grain configuration. It was found that heat treatment for one hour at 1350°C leads to large anisotropic grains (100-200μ in size), while a similar treatment at 1900°C produces more equiaxed grains having a slightly small size.

6.0 Needs and Opportunities in Ceramic Science

Personnel: W. D. Kingery

We are continuing to devote some effort to the initiative which was taken in the 1975 ERDA conference at M.I.T. on Needs and Opportunities in Ceramic Sciences; that is, to evaluate and discuss conceptual problems related to ceramic science and ceramic research, how these relate to energy requirements and opportunities, and how they relate to other areas of materials science.

In the past year we have served as a member of the DOE Steering Committee of the Council on Materials Science, participating in discussions to define subjects appropriate for review.

In an effort to increase the effectiveness of communication between basic science and its application, we have prepared an extensive review of Grain Boundary phenomena in Electronic Ceramics, which is described in Section 3.1 of this report. In addition, we have presented the plenary "Orton" lecture before the American Ceramic Society on the subject, "Social Needs and Ceramic Technology", in which it is concluded that the American Ceramic Society should be encouraged to take a more active role in bringing together industry-university-government programs and overcoming some of the perceived problems of anti-trust and tax situations which hamper that cooperation.

Scientific Staff

1. Senior Staff

Senior Staff	Time Devoted to Research			
W. D. Kingery, Ph.D.	11/1/79	to 5/31/80	50%	
Professor of Ceramics	7/1/80	to 8/31/80	100%	(2 summer months)
[redacted]	9/1/80	to 10/31/80	50%	
R. L. Coble, Sc.D.	11/1/79	to 5/31/80	50%	
Professor of Ceramics	6/1/80	to 6/31/80	100%	(1 summer month)
[redacted]	8/1/80	to 8/31/80	100%	(1 summer month)
	9/1/80	to 10/31/80	50%	
R. M. Cannon, Jr., Ph.D.	11/1/79	to 5/31/80	10%	
Assistant Professor of Ceramics	6/1/80	to 6/31/80	20%	(1 summer month)
[redacted]	8/1/80	to 8/31/80	20%	(1 summer month)
	9/1/80	to 10/31/80	10%	

Professors Kingery and Coble continued as Principal Investigators. In all cases, the research programs are organized, planned and carried out in close consultation with the Principal Investigators.

2. Graduate Students and Research Staff

D. Birnie
J. Blum
K. Cheng
Y. Chiang
W. Coblenz
L. Dolhert
N. Dudney
J. Dynys
R. French
J. Gambino
T. Gattuso
E. Giraldez
C. Handwerker
A. Henriksen
W. Hong
K. Kijima
T. Kuo-Wen
J. Schneibel
D. Sempolinski
Y. Tajima
W. Westphal
T. Yager
B. Zelinski

3. Support Staff

Secretary	1
Editorial Assistant	1
Administrative Assistant	1
Research Associates	3

4. Other Support by Federal Agencies Involving Senior Staff

W. D. Kingery	None		
R. L. Coble	None		
R. M. Cannon, Jr.	25%	NSF	5/1/79 to 4/30/80
	15%	DOD	7/1/79 to 6/30/80

We plan that all directly identified ceramic research and the entire research support of Professors Kingery and Coble continue to be provided by this contract and that no support of other agencies be solicited. There is no technical overlap between present contract work and that funded by the other government contracts.

5. Awards

Professor Kingery was selected as the Edward Orton Jr. Memorial Lecturer of the American Ceramic Society.

Professor Coble was selected as Distinguished Lecturer of the Northern Ohio Section of the American Ceramic Society.

6.0 Publications

6.1 Theses

W. S. Coblenz, "Physics of Sintering of Covalent Materials," Sc.D., M.I.T. Department of Materials Science and Engineering, September 1980

T. R. Gattuso, "Slow Defect Diffusion in KCl," Ph.D., M.I.T. Department of Materials Science and Engineering, September 1980

K. W. Cheng, "Kinetic Processes in Magnesium Oxide Single Crystals," Sc.D., M.I.T. Department of Materials Science and Engineering, February 1980

T. A. Yager, "Complex Clustering of Trivalent Cationic Solutes in MgO," Ph.D., M.I.T. Department of Materials Science and Engineering, February 1980

J. M. Driear, "Modification of the Permittivity of MgO by Aliovalent Solutes and Dislications," Sc.D., M.I.T. Department of Materials Science and Engineering, June 1980

Y. M. Chiang, "Grain Boundary Composition in Manganese Zinc Ferrites," S.B., Department of Materials Science and Engineering, June 1980

6.2 Papers published or accepted for publication

J. M. Dynys, R. L. Coble, W. S. Coblenz, and R. M. Cannon, "Mechanisms of Atom Transport during Initial Stage Sinering of Al_2O_3," Sintering Processes, Edited by G. C. Kuczynski, Plenum Publishing Corporation, 1980.

W. S. Coblenz, J. M. Dynys, R. M. Cannon, and R. L. Coble, "Initial Stage Solid State Sintering Models. A Critical Analysis and Assessment," Sintering Processes, Edited by C. G. Kuczynski, Plenum Publishing Corporation, 1980.

W. H. Gourdin and W. D. Kingery, "The Defect Structure of MgO Containing Trivalent Cation Solutes: Shell Model Calculations," J. Materials Science 14, 2053-73 (1979).

W. H. Gourdin, W. D. Kingery, and J. Driear, "The Defect Structure of MgO Containing Trivalent Cation Solutes: The Oxidation-Reduction Behavior of Iron," J. Materials Science 14, 2074-82 (1979).

A. F. Henriksen and W. D. Kingery, "Effects of Strain Energy on Precipitate Morphology in MgO," Ceramurgia International 5 [2], 56-60 (1979).

T. Mitamura, E. L. Hall, W. D. Kingery, and J. B. Vander Sande, "Grain Boundary Segregation of Iron in Polycrystalline Magnesium Oxide Observed by STEM," Ceramurgia International 5 [4], 131-136 (1979).

W. D. Kingery, T. Mitamura, J. B. Vander Sande and E. L. Hall, "Boundary Segregation of Ca, Fe, La and Si in MgO," J. Materials Science 14, 1766-67 (1979).

D. R. Sempolinski and W. D. Kingery, "Ionic Conductivity and Magnesium Vacancy Mobility in Magnesium Oxide," J. American Ceramic Society, in press.

D. R. Sempolinski, W. D. Kingery, and H. L. Tuller, "Electronic Conductivity of Single Crystalline Magnesium Oxide," J. American Ceramic Society, in press.

T. A. Yager and W. D. Kingery, "Laser-Heated High-Temperature EPR Spectroscopy," Review of Scientific Instruments, 51, 464-66 (1980).

W. D. Kingery, "Grain Boundary Phenomena in Electronic Ceramics," J. American Ceramic Society, in press.

W. D. Kingery, "Social Needs and Ceramic Technology," the 1980 Orton Lecture, Bull. American Ceramic Society, 59, 598 (1980).

6.3 Papers submitted for publication

T. A. Yager and W. D.Kingery, "The Kinetics of Clustering Reactions in Iron-Doped MgO," J. Materials Science.

T. A. Yager and W. D.Kingery, "The Equilibrium Defect Structure of Iron-Doped MgO in the Range 600°-1200°C," J. Materials Science.

Y. M. Chiang, A. F. Henriksen, W. D. Kingery and D. Finello, "Characterization of Grain Boundary Segregation in MgO," J. American Ceramic Society.

6.4 Lectures or papers presented or scheduled

R. L. Coble, "Defects in Al_2O_3," Colloquium at Pennsylvania State University, Pittsburgh, Penn., April 1980

R. L. Coble, "Grain Growth," Northern Ohio Section of the American Ceramic Society, Alumina Seminar, Cleveland, Ohio, March 1980

W. D. Kingery, "Grain Boundary Phenomena in Electronic Ceramics," Keynote address, International Symposium on Grain Boundary Phenomena in Electronic Ceramics, Annual Meeting of the American Ceramic Society, Chicago, April 27-30, 1980, to be published in Symposium Proceedings.

W. D. Kingery, "Social Needs and Ceramic Technology," the 1980 Orton Lecture, Annual Meeting of the American Ceramic Society, Chicago, April 27-30, 1980, Bulletin of the American Ceramic Society, in press.

Papers presented at the Annual Meeting of the American Ceramic Society, Chicago, Illinois, April 27-30, 1980

W. D. Kingery, "Grain Boundary Phenomena in Electronic Ceramics"

W. D. Kingery, "Social Needs and Ceramic Technology," 1980 Orton Lecture

T. A. Yager and W. D. Kingery, "Equilibrium Defect Structure of Iron-Doped MgO"

J. M. Driear and W. D. Kingery, "Modification of the Permittivity of MgO by Iron Solutes"

K. Kijima, W. D. Kingery, and Y. Tajima, "Auger Electron Spectroscopy Studies on Boron Doped Silicon Carbide"

K. W. Cheng and W. D. Kingery, "Redox Kinetics of Fe Ions in Single Crystal MgO"

T. A. Yager and W. D. Kingery, "Defect Structure of Quenched MgO Crystals Containing Trivalent Cationic Solutes"

K. W. Cheng and W. D. Kingery, "Behavior of Hydroxyl Defects in MgO at High Temperature"

N. J. Dudney and R. L. Coble, "Galvanic Cell Measurements with Ionic Probes"

W. S. Coblenz, R. L. Coble, and R. M. Cannon, "Role of Sintering Additives on Transport on Competitive Paths in Silicon and SiC"

C. A. Handwerker, R. L. Coble, and R. M. Cannon, "Grain Growth in MgO"

T. R. Gattuso and R. L. Coble, "Quenching of Lattice Defects in Alkali Halide Single Crystal"